MIT Libraries | DSpace@MIT

MIT Open Access Articles

A STEADY-STATE PICTURE OF SOLAR WIND ACCELERATION AND CHARGE STATE COMPOSITION DERIVED FROM A GLOBAL WAVE-DRIVEN MHD MODEL

Massachusetts Institute of Technology

A STEADY-STATE PICTURE OF SOLAR WIND ACCELERATION AND CHARGE STATE COMPOSITION DERIVED FROM A GLOBAL WAVE-DRIVEN MHD MODEL

R. Oran[1,2], E. Landi[1], B. van der Holst[1], S. T. Lepri[1], A. M. Vásquez[3,4], F. A. Nuevo[3,4], R. Frazin[1], W. Manchester[1], I. Sokolov[1], AND T. I. Gombosi[1]

[1] Atmospheric, Oceanic and Sciences, University of Michigan, 2455 Hayward, Ann Arbor, MI, 48109, USA; oran@umich.edu
[2] Earth, Atmospheric, and Planetary Sciences, Massachusetts Institute of Technology, 77 Massachusetts Ave., Cambridge, MA, 02139, USA
[3] Instituto de Astronomía y Física del Espacio (IAFE), CONICET-UBA, CC 67—Suc 28, (1428) Buenos Aires, Argentina
[4] Facultad de Ciencias Exactas y Naturales (FCEN), Universidad de Buenos Aires, Argentina

ABSTRACT

The higher charge states found in slow (<400 km s^{-1}) solar wind streams compared to fast streams have supported the hypothesis that the slow wind originates in closed coronal loops and is released intermittently through reconnection. Here we examine whether a highly ionized slow wind can also form along steady and open magnetic field lines. We model the steady-state solar atmosphere using the Alfvén Wave Solar Model (AWSoM), a global MHD model driven by Alfvén waves, and apply an ionization code to calculate the charge state evolution along modeled open field lines. This constitutes the first charge state calculation covering all latitudes in a realistic magnetic field. The ratios O^{+7}/O^{+6} and C^{+6}/C^{+5} are compared to in situ *Ulysses* observations and are found to be higher in the slow wind, as observed; however, they are underpredicted in both wind types. The modeled ion fractions of S, Si, and Fe are used to calculate line-of-sight intensities, which are compared to Extreme-ultraviolet Imaging Spectrometer (EIS) observations above a coronal hole. The agreement is partial and suggests that all ionization rates are underpredicted. Assuming the presence of suprathermal electrons improved the agreement with both EIS and *Ulysses* observations; importantly, the trend of higher ionization in the slow wind was maintained. The results suggest that there can be a sub-class of slow wind that is steady and highly ionized. Further analysis shows that it originates from coronal hole boundaries (CHBs), where the modeled electron density and temperature are higher than inside the hole, leading to faster ionization. This property of CHBs is global and observationally supported by EUV tomography.

Key words: magnetohydrodynamics (MHD) – methods: numerical – Sun: corona – Sun: heliosphere – techniques: spectroscopic – turbulence

1. INTRODUCTION

The formation of the solar wind and its acceleration through interplanetary space pose some of the central outstanding problems in solar physics. These include identifying the processes by which the solar wind is formed and accelerated, and explaining how these processes produce the observed three-dimensional (3D), time-dependent distributions of plasma properties and composition. The solar wind has been measured and analyzed extensively over the past few decades, and considerable amounts of data have been gathered. This has led to the identification of distinctly different solar wind flows, commonly classified as the fast (~700 km s^{-1}) or slow (~300–400 km s^{-1}) solar wind (see, e.g., McComas et al. 2003). While it is generally accepted that the fast wind originates from coronal holes (CHs), the markedly different chemical composition and temporal variability of the slow wind have led to an ongoing and vigorous debate regarding its source region and formation mechanism (Kohl et al. 2006; Suess et al. 2009; Abbo et al. 2010; Antiochos et al. 2011, 2012; Antonucci et al. 2012).

The abundances of heavy elements in the solar atmosphere and their ionization state have played a central role in testing theories of solar wind formation. The abundances of elements heavier than helium, relative to that of hydrogen, are lower than 0.001 everywhere in both the solar wind and solar corona (e.g., Feldman et al. 1992; Asplund et al. 2009; Caffau et al. 2011), and therefore their contribution to the large-scale dynamics is negligible. However, their response to the local state of the plasma in which they are embedded makes them useful tracers

of the conditions in different regions. Indeed, both their relative abundances and their ionization status vary when observed in different regions of the corona and the wind.

The abundances of certain elements exhibit coronal abundances that differ from the corresponding photospheric values, depending on the element's first ionization potential (FIP) (see Feldman & Laming 2000; Feldman & Widing 2003, and references therein). The ratio of coronal to photospheric abundances is called the FIP bias. Closed-field structures such as helmet streamers and active regions exhibit an FIP bias between 2 and 4 for low-FIP (<10 eV) elements, while CHs do not (Feldman & Widing 2003). In situ solar wind measurements show that different wind streams also exhibit different FIP biases: the fast wind exhibits elemental abundances characteristic of the photosphere and CHs (Zurbuchen et al. 1999, 2002; von Steiger et al. 2001), while the slow wind exhibits FIP-biased abundances similar to that of closed coronal loops (Feldman & Widing 2003). To date, there is still no clear and conclusive picture that explains the observed FIP bias in both the corona and the fast wind, but several promising theories are being developed (see Laming 2009, 2012 for a review of this active research area).

In contrast to the FIP bias, the basic mechanisms controlling heavy-element ionization are well understood. As the ions propagate away from the Sun, they undergo ionization and recombination due to collisions with free electrons. The collision rate depends on the electron density, while the ionization and recombination rate coefficients can be derived

from atomic physics, provided that the energy of the electrons is known. Due to the decrease of electron density with distance from the Sun, at a certain distance the plasma becomes collisionless and ionization and recombination processes effectively stop. At this point the charge state distribution of the element is said to "freeze-in," which usually occurs at distances between 1.5 and $4\,R_\odot$, depending on the ion considered (Hundhausen et al. 1968). The charge state distribution, which is routinely analyzed by in situ measurements in the heliosphere, therefore contains information about the wind evolution very close to the Sun. These measurements revealed that the slow wind consistently exhibits higher ionization than the fast wind, suggesting that these flows undergo different evolution at their origin. The charge states measured in the fast wind are compatible with an electron temperature at the lower corona of ~1.0 MK, similar to that occurring in CHs (e.g., Gloeckler et al. 2003; Zurbuchen 2007), while the charge states in the slow wind are generally higher and may be compatible with higher coronal electron temperatures, as found in closed field regions (e.g., Zurbuchen et al. 2002; Gloeckler et al. 2003).

The correspondence between slow wind composition and the properties of coronal loops has led to the hypothesis that the slow wind plasma originates in the hotter and denser closed field region in the corona. Models of this type are discussed in Section 1.1. Here we briefly note that if the source region of the slow wind is closed coronal loops, then there must be a mechanism by which the plasma is released. This is usually assumed to happen through magnetic reconnection, making these models inherently time dependent with a dynamically changing magnetic field configuration. In this paper, in contrast, we focus on a steady-state picture of solar wind formation, in which both fast and slow flows are accelerated solely along open field lines. In particular, we examine whether a steady wind that is heated and accelerated by Alfvén waves can explain the observed charge state distributions, both in the solar corona and in the fast and slow solar wind. For this purpose, we use a global magnetohydrodynamics (MHD) computational model driven by Alfvén waves to predict the plasma flow properties and magnetic field starting from the solar transition region up to a distance of 2 AU. We then calculate the charge state evolution of heavy elements as they flow along modeled open field lines and undergo ionization and recombination. In order to study both slow and fast wind flows, we perform these calculations at all latitudes. As we describe in more detail below, elemental abundances and dynamic processes are not included in the simulations. Nonetheless, comparing the modeled charge state distributions to available in situ and remote observations will allow us to gain further insight into how well the MHD model describes the wind evolution, and to extend our current understanding of how and where the slow wind is formed.

1.1. Theoretical Models of Solar Wind Formation

A wide range of theoretical models relate the distribution of fast and slow wind speeds to the steady state magnetic field geometry and the expansion of open magnetic flux tubes (Suess 1979; Kovalenko 1981; Withbroe 1988; Wang & Sheeley 1990; Roussev et al. 2003; Cranmer & van Ballegooijen 2005; Suzuki 2006; Cohen et al. 2007; Cranmer et al. 2007; van der Holst et al. 2010). In this picture, both the fast and slow wind flows along static open field lines, and the slow wind originates from the outer regions of CHs, where the

expansion is largest. In the context of these models, the term CHs simply refers to the steady open field regions. This definition may lead to some ambiguity: in solar observation literature the term CHs often refers to those regions that appear dark in imaging of coronal emission. Thus, from the observational perspective, CHs are only a subset of open field line regions, and their boundaries may not overlap the open field boundaries. In this paper we adopt the former definition and use the terms CHs and open field line regions interchangeably.

It is often regarded that static expansion models cannot explain the different chemical composition found in the slow and fast wind. In these models both wind types originate in CHs, and they do not include an explicit mechanism that affects the chemical composition of the plasma. However, work presented in Cranmer et al. (2007) showed that variations in charge states and elemental abundance between the fast and slow wind could occur for a wind model with a static magnetic field. There, the charge states were directly calculated from the steady-state wind parameters, while the elemental abundances were obtained by adopting the fractionation mechanism suggested by Laming (2004). They were able to reproduce some of the main trends in the observations, based on an idealized magnetic field geometry. It should be noted, however, that pinning down the fractionation mechanism itself is still the subject of active research. Further, predicting elemental fractionation from steady-state models is limited by the fact that the FIP bias observed in coronal loops seems to change with the age of the loop (e.g., Feldman & Widing 2003), suggesting that time-dependent effects may be important.

An alternative approach to static models suggests that the slow wind originates in the closed field regions, which already contain highly ionized and FIP-biased plasma. In models of this type the plasma is dynamically and intermittently released into space due to reconnection between open and closed field lines, although the details and the location of the reconnection process vary (e.g., the Interchange Reconnection Model, Fisk et al. 1998; Fisk 2003; Fisk & Zhao 2009; the Streamer-Top Model, Wang et al. 2000; the S-web Model, Antiochos et al. 2007, 2011, 2012). Dynamic release models can also potentially explain the different levels of fluctuations observed in the fast and slow wind. The flow properties of the fast wind are relatively steady (e.g., McComas et al. 2000), while those measured in the slow wind are highly variable in comparison (Bame et al. 1977; Schwenn & Marsch 1990; Gosling 1997; McComas et al. 2000). Similarly, the chemical composition of the fast wind is relatively steady (Geiss et al. 1995; von Steiger et al. 1995; Zurbuchen 2007), while that of the slow wind is highly variable (Zurbuchen & von Steiger 2006; Zurbuchen 2007). These models offer a natural explanation for this variability, since they imply that the slow wind is formed in a series of discrete and localized release events. However, dynamic release models are limited by the localized and time-dependent nature of the wind formation mechanism, which is difficult to incorporate into global simulations with a realistic magnetic field.

Another class of solar wind acceleration models are wave-driven models. Alazraki & Couturier (1971) and Belcher (1971) have suggested that low-frequency Alfvén waves can accelerate the wind due to gradients in the wave pressure and heat the corona through wave dissipation. The source of the wave energy is usually assumed to be turbulent motions in the photosphere and chromosphere. An observational support of

this picture was given in de Pontieu et al. (2007), who analyzed *Hinode* observations of chromospheric fluctuations and found them to be Alfvénic in nature. However, a significant amount of the wave energy will be reflected in the transition region due to the steep density gradient there (Ferraro & Plumpton 1958). Using radiative-MHD simulations, de Pontieu et al. (2007) found that between 3% and 15% of the Poynting flux they observed in the chromosphere will be transmitted into the corona, with a resulting energy flux that is sufficient to sustain the corona and solar wind. Further theoretical work (e.g Chandran & Hollweg 2009; van Ballegooijen et al. 2011) was aimed at simulating in detail the propagation, reflection, and subsequent turbulent dissipation of Alfvén waves in representative flux tube geometries. Specifically, van Ballegooijen et al. (2011) found the simulated wave amplitudes in the chromosphere, created by repeated reflections, to be consistent with the values determined from observations by de Pontieu et al. (2007). These works suggest that Alfvén waves may be a plausible conduit for the energy required for heating and acceleration in the solar environment. Indeed, Alfvénic perturbations are ubiquitous in the solar environment and have been observed in the photosphere, chromosphere, coronal structures, and the solar wind at Earth's orbit (see Banerjee et al. 2011; McIntosh et al. 2011).

Alfvén waves were incorporated into several MHD models of the solar atmosphere in an attempt to explain the observed properties of the solar wind and corona (e.g., Usmanov et al. 2000; Usmanov & Goldstein 2003; Cranmer & van Ballegooijen 2005; Cranmer et al. 2007; van der Holst et al. 2010; Evans et al. 2012; Usmanov et al. 2012; Oran et al. 2013; Sokolov et al. 2013; Lionello et al. 2014a, 2014b; van der Holst et al. 2014, to name a few). These models were able to describe the large-scale features of the corona and the wind, but for the large part did not explicitly address the wind's composition (except Cranmer et al. 2007; Cranmer 2014, which will be discussed below) or the temporal variability.

1.2. The Goal and Context of This Paper

The goal of this work is twofold: First, we wish to examine whether a solar wind model in which the wind is accelerated by Alfvén waves can explain the charge state distributions observed in both the corona and the wind. Second, we address the question of whether a solar wind that originates solely from CHs and propagates along static open magnetic field lines can lead to the formation of higher charge states in slow flows compared to fast flows, without invoking dynamic release from the closed field region.

We use the Alfvén Wave Solar Model (AWSoM, Oran et al. 2013; Sokolov et al. 2013; van der Holst et al. 2014), which extends from the top of the transition region up to 2 AU. The model solves the two-temperature (electrons and protons) MHD equations coupled to wave transport equations of parallel and anti-parallel Alfvén waves. Wave propagation and dissipation are treated self-consistently in both open and closed field regions, as described in Sokolov et al. (2013). Oran et al. (2013) showed that for a solar minimum configuration, the model can reproduce remote observations of the lower corona simultaneously with the large-scale distribution of wind speeds observed by *Ulysses* at 1–2 AU.

We take advantage of the steady-state simulation of the solar atmosphere previously presented and validated in Oran et al. (2013) as a basis for modeling charge state evolution and comparing the results to in situ and remote observations. The simulation was constrained by a synoptic map of the photospheric magnetic field observed during Carrington Rotation (CR) 2063, which took place during solar minimum. The electron density, temperature, and speed from the MHD simulation are used as input to a charge state evolution model (Michigan Ionization Code (MIC), Landi et al. 2012b) that calculates the ionization status of an element at any point along the wind trajectory. We calculate the evolution of C, O, S, Si, and Fe charge states, in order to compare the results to as many available observations as possible, both in the corona and in the wind.

The steady-state simulations presented here cannot describe dynamic release of material from closed field structures. In fact, in a static magnetic field both the slow and fast wind must originate from CHs and flow solely along open field lines. In this sense, the simulation presented here can be grouped with the expansion models discussed in Section 1.1. Antiochos et al. (2012) argued that expansion models cannot give a complete picture of solar wind formation, as they cannot explain the different composition and the large temporal fluctuations observed in the slow wind. By combining static models with appropriate charge state and fractionation models, one can attempt to reproduce the slow/fast variations in composition, at least for a steady-state configuration. Even with these additions, a static wind model indeed cannot explain the observed fluctuations of any of the slow wind properties. However, the question still remains: can a wind accelerated by Alfvén waves along static open field lines possess a large-scale variation in charge states, solely because ions flowing along different trajectories will encounter different plasma conditions?

Several authors have derived the charge state evolution in static wave-driven MHD models. Cranmer et al. (2007) calculated the charge state evolution of O ions and found the resulting ion fractions to be in qualitative agreement with *Ulysses* observations. The agreement was greatly improved when electron κ distributions were introduced into the model by Cranmer (2014). The κ distributions worked to increase the ionization levels compared to those obtained from a Maxwellian electron distribution. The MHD model in Cranmer et al. (2007) and Cranmer (2014) was based on a prescribed axially symmetric magnetic field topology that is not derived self-consistently with the plasma and wave field. This limits the analysis to idealized flux tube geometries and cannot include more complex structures. Jin et al. (2012) calculated the frozen-in charge state distributions using a 3D MHD model with a realistic and self-consistent magnetic field. The calculation was performed over a few representative field lines and was not aimed at addressing the variation between fast and slow wind streams. Here we present the first calculation of charge state distributions covering all heliographic latitudes, in a realistic, fully three-dimensional and self-consistent magnetic field configuration. This allows us to (1) examine how the modeled frozen-in distributions vary with terminal wind speed, (2) study the evolution below the freeze-in height, and (3) compare the results with observations performed in the same time period covered by the photospheric magnetogram driving the simulation. Predicting the charge state evolution of several heavy elements allows us to better constrain the validity of our results.

The modeled frozen-in distributions for O and C will be directly compared to in situ measurements performed by the

Solar Wind Ion Composition Spectrometer (SWICS, Gloeckler et al. 1992) on board *Ulysses* taken during its third polar scan at a distance of 1–2 AU. In the lower corona, on the other hand, information about the ionization state can only be gained from the observed emission associated with the different ions. We derive synthetic line intensities for S, Si, and Fe ions from the model and compare them to remote observations made by the Extreme-ultraviolet Imaging Spectrometer (EIS, Culhane et al. 2007) on board *Hinode*. Several spectral lines corresponding to different ionization stages are used, which allows us to examine the modeled ionization in detail. The simultaneous comparison to both remote and in situ observations allows us to test the predicted charge states at both ends of the wind trajectory (Landi et al. 2012a). This diagnostic approach was used by Landi et al. (2014) to test predictions of three theoretical models, including the AWSoM model, by applying the MIC code to a field line stretching along the center of a polar CH in an ideal dipole field. The strength of the 3D nature of the AWSoM-MIC simulations presented here is that we can calculate the charge states and their emission at every point along the line of sight (LOS), allowing us to produce synthetic emission profiles without the need to make simplifying assumptions about the spatial variation of these properties. This makes for a more rigorous model-data comparison.

Finally, we note that this work does not address the variation of elemental abundances observed in the fast and slow wind. Describing the formation of the FIP bias in an MHD model will require (1) a multi-fluid description to describe the evolution of each element; (2) the inclusion of an elemental fractionation mechanism responsible for the FIP bias, which as of yet has not been conclusively identified; and (3) a time-dependent description of coronal morphology. The last requirement stems from the fact that the FIP bias is known to vary with the age of a coronal loop, i.e., the time elapsed since its emergence from the chromosphere (e.g., Feldman & Widing 2003). A steady-state model driven by a synoptic magnetogram of the photospheric field cannot account for temporal changes. In addition, the FIP bias is largely active in lower and cooler regions of the solar atmosphere, and proper modeling of its creation would require a realistic model of the chromosphere, which is not included in the present AWSoM model. For these reasons, we defer the question of elemental abundances to future work and only address the charge state composition.

This paper is organized as follows. The theory of charge state evolution and the MIC code are described in Section 2. The AWSoM model and the steady-state simulation used in this paper are presented in Section 3. We discuss how the AWSoM simulation results were used to drive the ionization code in Section 4. The method of creating synthetic emission from the AWSoM-MIC results is described in Section 5. The in situ and remote observations used in this work are presented in Section 6. We present the model results and their comparison to the observations in Section 7. Section 8 discusses the main result of this paper, i.e., the formation of higher charge states in the modeled steady slow wind. We describe the different source regions of these wind streams and discuss how the plasma properties close to the Sun explain the increased ionization. We show that the main component of this steady slow wind, which comes from the boundaries of CHs, is highly ionized due to enhanced electron density and temperature compared to deeper inside the holes. We present observational

evidence of this enhancement using an EUV tomographic reconstruction of the lower corona. Section 9 summarizes the results and discusses their possible interpretations and implications to understanding solar wind formation.

2. CHARGE STATE EVOLUTION MODEL

2.1. Evolution along Field Lines

As heavy ions are accelerated away from the Sun, they undergo ionization and recombination due to collisions with the electrons, at rates that depend on the local electron density, N_e, and temperature, T_e. The speed of the ions determines how much time they spend at a given location; if the speed is sufficiently high, the ions will not reach local ionization equilibrium. In this case the population of each charge state can only be determined by taking into account the flow properties along the entire trajectory. The rate of change (in the rest frame) of the population of element y at charge state m is given by the following equation:

$$\frac{\partial N_y y_m}{\partial t} + \nabla \cdot \left(y_m N_y \boldsymbol{u}_{y_m} \right) = N_e N_y \Big[y_{m-1} C_{m-1}(T_e)$$
$$+ y_{m+1} R_{m+1}(T_e) - y_m C_m(T_e) - y_m R_m(T_e) \Big],$$
$$\sum_m y_m = 1, \tag{1}$$

where N_y is the total number density of element y, y_m is the fraction of element y in charge state m, R_m and C_m are recombination and ionization rate coefficients, respectively, and $\boldsymbol{u}_{y_m}$ is the ion velocity. The first two terms on the right-hand side describe the creation of ions with charge state m due to ionization from a lower charge state and recombination from a higher charge state, while the last two terms describe losses due to ionization and recombination of ions with charge m into higher and lower charge states, respectively. Ionization and recombination are assumed to be due to binary reactions between ions and electrons, namely, direct collisional ionization, excitation-autoionization, radiative recombination, and dielectronic recombination. Three-body recombination (as well as photoionization) is negligible in the solar atmosphere (Hundhausen et al. 1968). Thus, in Equation (1) the number of reactions occurring per unit volume per unit time is proportional to the product of the concentrations of the reacting particles, $N_e N_y y_m$. The recombination and ionization rate coefficient depend on the electron energy and are calculated using the CHIANTI 7.1 Atomic Database (Dere et al. 1997; Landi et al. 2013). The rate coefficients in CHIANTI are largely based on the ionization rates compiled by Dere (2007) and the recombination rates reviewed by Dere et al. (2009).

Equation (1) constitutes a system of continuity equations of the number density of each charge state, which are coupled through the ionization and recombination source terms. If we assume that all ions flow with the same velocity, $\boldsymbol{u}$, we can take the sum of the equations over all m for each element y and obtain a continuity equation for the total elemental number density N_y:

$$\frac{\partial N_y}{\partial t} + \nabla \cdot \left(N_y \boldsymbol{u} \right) = 0. \tag{2}$$

Equation (2) can now be used to eliminate derivatives involving N_y on the left-hand side of Equation (1). For the case of steady-state evolution, we obtain the following system of equations for each charge state (Hundhausen et al. 1968; Ko et al. 1997; Landi et al. 2012a):

$$(\boldsymbol{u} \cdot \nabla) y_m = u_\parallel \frac{dy_m}{ds} = N_e \Big[y_{m-1} C_{m-1}(T_e)$$
$$+ y_{m+1} R_{m+1}(T_e) - y_m C_m(T_e) - y_m R_m(T_e) \Big],$$
$$\sum_m y_m = 1, \tag{3}$$

where $u_\parallel$ is the speed parallel to the flow line and ds is the path length. This system of equations is solved numerically by the MIC code using a fourth-order Runge–Kutta method with an adaptive step size that limits the change in any charge state fraction to a maximum of 10%. The boundary conditions for y_m at the base of the flow line are derived assuming ionization equilibrium.

The MIC model requires information about the electron density and temperature, as well as the wind speed, in order to solve Equation (3). Since we are interested in the large-scale steady-state solution, the wind properties at any point are constant in time. In this work, these quantities are taken from the MHD solution given by the AWSoM model. In the MHD approximation, the plasma flows parallel to magnetic field lines in the rest frame, which in our case is the frame co-rotating with the Sun. We extract the needed quantities along simulated open magnetic field lines, and $u_\parallel$ is taken with respect to the co-rotating frame. Finally, we note that the AWSoM model equations do not describe separate ion velocities, and it is therefore assumed that the ions move with the same speed as the plasma. The same assumption was made when deriving Equation (3), and thus the bulk velocity in the MHD solution is consistent with that appearing in the charge state evolution equations. This assumption of equal ion speeds does not strictly hold at all locations in the solar atmosphere, and future work may take differential ion speeds into account.

2.2. Role of Supra-thermal Electrons

Supra-thermal electrons can have a considerable effect on charge state evolution, as their energy will modify the ionization rate coefficients. As of yet, there is no direct observational evidence of their presence in the lower corona, and the subject is still under debate (see Cranmer 2009 for a review). However, a supra-thermal population can potentially reconcile the discrepancy between the observed charge states and coronal temperatures. Several studies used the observed frozen-in charge states in the fast wind in order to put constraints on the electron temperature low in CHs (see, e.g., Geiss et al. 1995; Ko et al. 1997). When a purely Maxwellian electron population was assumed, the coronal temperatures that can explain the in situ observations were about 50% higher than those derived from spectral observations below the freeze-in height. Esser & Edgar (2000) showed that this discrepancy can be resolved if an additional small population of supra-thermal electrons is present. Differential ion speeds may have a similar effect on the frozen-in charge states (Ko et al. 1998; Esser & Edgar 2001), but this mechanism is beyond the scope of the present work. Laming & Lepri (2007) showed that supra-thermal electrons can be created due to parallel heating

by lower hybrid wave damping, giving rise to a κ distribution function for the electrons, which can explain the observed charge states. Cranmer (2014) presented a first-principle transport model for electrons in the lower corona and showed that the resulting electron distribution function is somewhere between a $\kappa = 10$ and $\kappa = 25$ distribution. Feldman et al. (2007) estimated the energy content of supra-thermal electrons in an active region and found that less than 5% of the electron population can have energies above 0.91 keV and less than 2% can have energies above 1.34 keV in active regions.

Following these previous efforts, in this work we consider the charge state evolution due to a single-temperature plasma, as well as a plasma with an additional hotter electron population, in order to evaluate their contribution. We assume that 2% of the electrons belong to a second Maxwellian distribution at $3\,\mathrm{MK} \approx 0.25\,\mathrm{keV}$. These parameters were chosen empirically, as we describe in Section 7. Ideally, a full parametric study of these values should be performed, guided by observations. Such a study is beyond the scope of this work. Nonetheless, incorporating the supra-thermal electrons in the simulation serves as a proof of concept, to determine whether they can, at the same time,

1. affect the predicted charge state composition and improve the agreement with in situ observations; and
2. produce observable signatures in coronal emission, with an overall effect that is consistent with observed spectra.

In order to accomplish this, we need to apply two sets of ionization rate coefficients when solving Equation (3): one in which only the thermal electron population is taken into account, and another where both the thermal and supra-thermal populations are considered. Supra-thermal electrons will also impact the emissivity of the plasma, and therefore we take them into account when calculating synthetic emission from the model, as we describe in Section 5.

3. THE AWSoM MODEL DESCRIPTION

The AWSoM model is a 3D computational model of the solar environment, extending from the transition region into inter-planetary space. It solves the extended-MHD equations (with separate electron and proton temperatures) coupled to wave transport equations for low-frequency Alfvén waves, propagating parallel or anti-parallel to the magnetic field. The coupled equations allow for a self-consistent description of coronal heating and wind acceleration, where wave dissipation heats the plasma and wave-pressure gradients accelerate it. Wave dissipation is the only heating mechanism, and the dissipated energy is partitioned between the protons and electrons. The separate electron and proton temperatures enable us to include non-ideal MHD processes: field-aligned electron heat conduction, radiative cooling, and thermal coupling between the electrons and protons.

A detailed description of the model and its development was presented in Sokolov et al. (2013), Oran et al. (2013), and van der Holst et al. (2014). The AWSoM simulation used in this work is described in detail in Oran et al. (2013). The wave dissipation is assumed to be a result of fully developed turbulent cascade (Matthaeus et al. 1999) due to counter-propagating waves in closed field regions and wave reflections in open field regions. Wave reflections, which are in general frequency dependent, are not described explicitly (as was done, for example, in Cranmer & van Ballegooijen 2005; Cranmer

et al. 2007). Rather, the model adopts the approach proposed by Hollweg (1986), in which a Kolmogorov-type dissipation rate is assumed. The Kolmogorov approach, originally developed for open magnetic flux tubes, was generalized to both open and closed field lines in Sokolov et al. (2013). The dissipation mechanism was analyzed in detail in Sokolov et al. (2013) and Oran et al. (2013), and its predictions of the wave amplitude in the corona and solar wind were shown to be consistent with observation both in the solar wind (Oran et al. 2013) and in the lower corona (Oran et al. 2014) during solar minimum. Jin et al. (2013) simulated a more complex magnetic topology that took place during the ascending phase of the solar cycle. They successfully simulated the propagation and evolution of a coronal mass ejection, whose modeled evolution was validated against white-light observations of the outer corona.

In this work we use an AWSoM simulation for CR2063, which took place between November 4 and December 1 in 2007. The boundary conditions for the radial magnetic field are derived from an LOS synoptic magnetogram obtained for that period by the Michelson Doppler Interferometer (MDI) instrument on board the *Solar and Heliospheric Observatory* (*SOHO*) spacecraft (Scherrer et al. 1995). The simulation set-up, input parameters, and comparison to remote and in situ observations are described in detail in Oran et al. (2013).

4. COORDINATED OBSERVATIONS AND FIELD LINE SELECTION

We take advantage of high-resolution observations performed by the EIS instrument on board *Hinode* taken during CR2063, on 2007 November 16, at 11:47:57UT, observing the north polar CH. This particular set of EIS observations was chosen since it includes bright and isolated emission lines from several charge states of Fe, two charge states of Si, and one charge state of S. In the same period, *Ulysses* was performing its third and last polar scan, covering almost all latitudes in a period of a little over a year.

Modeling the charge state evolution for all ions in the entire 3D domain is computationally expensive, and therefore we only solve the charge state evolution along selected field lines, depending on the specific need:

1. For comparison with remote observations, we chose the field lines that intersect the EIS LOS. Field lines at $1°$ spacings in the northern hemisphere were extracted; although they lie in the same meridional plane at altitudes covered by the EIS slit above the north polar CH, they reach slightly different longitudes at their footpoints, due to the complex magnetic topology.
2. For comparison with *Ulysses* observations, the MIC solution is obtained for field lines that reach the same meridional plane at 1.8 AU, at all latitudes at $1°$ spacings. Since AWSoM is driven by a synoptic magnetogram, changes in the solar magnetic field during *Ulysses's* year-long polar scan are not simulated. The comparison should be regarded as a qualitative examination of how well the model reproduces the large-scale structure of the frozen-in charge states during solar minimum. In this case tracking the solution along the field lines reaching the exact *Ulysses* trajectory is not needed, and it suffices to cover all latitudes.

The geometry is shown schematically in Figure 1. The black curves are magnetic field lines, while the solar surface is colored by the radial magnetic field and the gray surface represents the location of the current sheet. The direction of the EIS LOS is shown by the yellow arrow. The blue arrows represent the general direction of *Ulysses* polar pass, although the details of the trajectory itself are not represented in this figure. Note that only the open field lines were used to obtain a solution from MIC, and closed field lines are shown here for clarity.

5. CALCULATING NON-EQUILIBRIUM SYNTHETIC LINE-OF-SIGHT EMISSION

The emission of a volume of plasma at a given spectral line due to an electronic transition from an upper level j to a lower level i depends on the contribution function, $G_{ji}(N_e, T_e)$, defined as

$$G_{ji}(N_e, T_e) = A_{ji} \frac{N_j(X^{+m})}{N(X^{+m})} \frac{N(X^{+m})}{N(X)} \frac{N(X)}{N(H)} \frac{N(H)}{N_e} \frac{1}{N_e}, \quad (4)$$

where G_{ji} is measured in units of photons $cm^3\ s^{-1}$. X^{+m} denotes the ion of the element X at ionization state $+m$, which is responsible for the emission. The factors of the form $N(z)$ denote abundances of z, where z can represent either an element or an ion. H denotes hydrogen. The term $N_j(X^{+m})$ is the population of the ion X^{+m} that is in the upper state j. A_{ji} is the Einstein coefficient for spontaneous emission for the transition $j \to i$.

The separate terms of the contribution function are determined from the macroscopic state combined with atomic physics. A full description of these terms appears many times in the literature and will not be repeated here (see, e.g., Landi et al. 2012a). $G_{ji}(N_e, T_e)$ is often calculated assuming ionization equilibrium in a thermal population of electrons. To obtain synthetic emission that truly reflects the model results, the contribution function must be modified from the equilibrium values as follows:

1. *Ion Fractions*: The ratio $N(X^{+m})/N(X)$ is the abundance of the ion X^{+m} relative to the abundance of the element X (second ratio on the right-hand side (rhs) of Equation (4)). We hereafter refer to this ratio as the ion fraction. In the case of a moving plasma, the ions may not have sufficient time to reach ionization equilibrium. Thus, in calculating the synthetic emission, we must use the ion fractions predicted by MIC (Equation (3)), instead of ionization-equilibrium fractions. We note that the MIC-predicted ion fractions themselves will be different with or without the presence of supra-thermal electrons (see Section 2.2). This is because the higher energies of the supra-thermal electrons will result in different ionization and recombination rate coefficients used in Equation (3).
2. *Level Populations:* The ratio $N_j(X^{+m})/N(X^{+m})$ is the relative level population of X^{+m} ions at level j (first ratio on the rhs of Equation (4)), and it depends on the density and energy distribution of the electrons. The level population will be affected by the presence of supra-thermal electrons, as the additional energy they carry will change the collisional excitation/de-excitation rates.
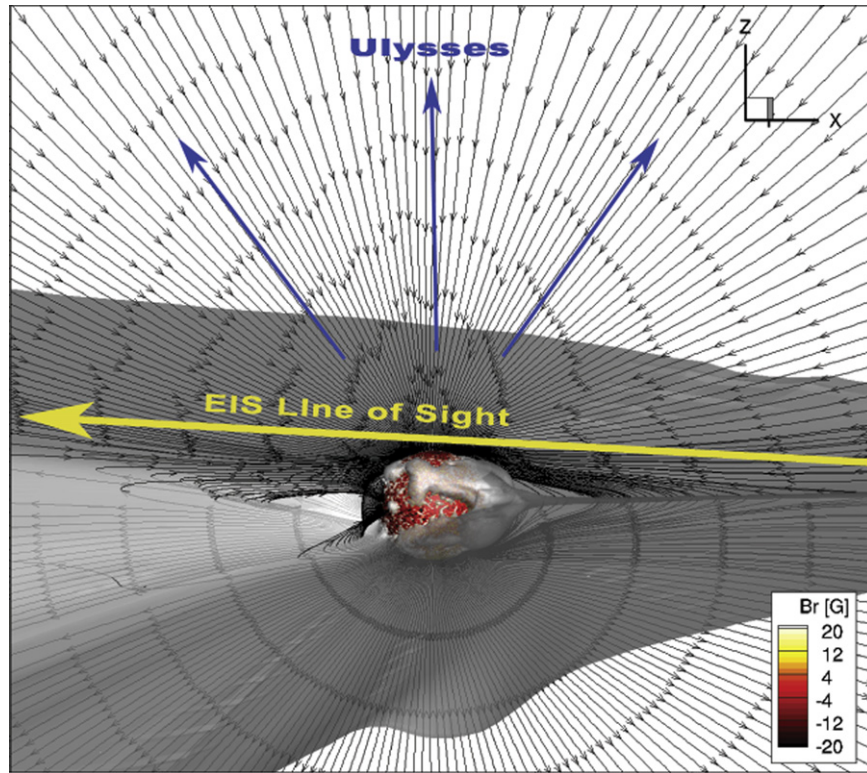
Figure 1. Geometry used for comparing model results with *Ulysses* and EIS coordinated observations. Black stream lines show the magnetic field lines extracted from the AWSoM simulation for CR2063. Wind parameters along the open field lines were used as input to MIC. Labeled arrows mark the direction of the EIS LOS and the general direction of *Ulysses* during its polar scan. The solar surface is colored by the radial magnetic field obtained from a synoptic MDI magnetogram. The gray surface represents the heliospheric current sheet, where the radial magnetic field is zero.

The level population in any computational volume element can be calculated by combining the modeled electron density and temperature with the CHIANTI atomic database, which can take in either a single-temperature electron population or a population with additional supra-thermal electrons. In contrast, the MIC ion fractions need to be specified directly for each volume element in the model. In all these calculations, we used the photospheric elemental abundances from Caffau et al. (2011).

Once the contribution function is calculated at every point along the LOS, the total observed flux in the optically thin limit is given by the integral

$$F_{\mathrm{tot}} = \int \frac{1}{4\pi d^2} G_{ji}(N_e, T_e) N_e^2 \, dV, \qquad (5)$$

where d is the distance of the instrument from the emitting volume dV. F_{tot} is measured in units of photons cm^{-2} s^{-1}. This volume integral can be replaced by a line integral by observing that $dV = A\,dl$, where A is the area observed by the instrument and dl is the path length along the LOS. The electron density, electron temperature, and contribution function predicted by AWSoM-MIC are interpolated from the field lines intersecting the LOS into a uniformly spaced set of points along each observed LOS. This procedure ensures that the integration is second-order accurate.

6. OBSERVATIONS

6.1. Ulysses In Situ Charge States

We use the charge state measurements obtained by the SWICS instrument on board *Ulysses* between 2007 February 15 and 2008 January 15. This period overlaps the time at which the synoptic magnetogram for CR2063 and the remote EIS observations were obtained. The start and end dates were chosen so that the widest range of latitudes is included in the data set. The charge state ratios of O^{7+}/O^{6+} and C^{6+}/C^{5+} and the average charge state of Fe, $\langle Q \rangle_{\mathrm{Fe}}$, are publicly available through ESA's *Ulysses* data system, and their calculation from the raw measurements is described in von Steiger et al. (2000). The statistical accuracy of the measurements is estimated to be 10%–25% (*Ulysses*/SWICS Heavy Ion Composition Data: User's Recipe, by T. Zurbuchen and R. von Steiger, 2011).

The oxygen and carbon charge state ratios are sensitive to the electron temperature in the inner corona (up to the freeze-in height of 1.5–2 $R_\odot$), and they are often used to distinguish between different solar wind types and to study their source regions (e.g., Zurbuchen et al. 2002; Zhao et al. 2009, 2014). The charge states of Fe have a freeze-in height of $\sim$4 $R_\odot$ and were used to study the wind evolution in the outer corona (e.g., Lepri et al. 2001; Lepri & Zurbuchen 2004; Gruesbeck et al. 2011). However, the magnitude of $\langle Q \rangle_{\mathrm{Fe}}$ does not change by much when measured in the fast and slow wind (Lepri et al. 2001), and its behavior in the two wind types only differs in the level of temporal fluctuations. We therefore focus on

Table 1
Selected EIS Emission Lines

Ion Name	Wavelength	$F_{\rm scatt}$	$R_{\rm max}$
	(Å)	(erg cm^{-2} s^{-1} sr^{-1})	($R_\odot$)
Fe VIII	185.213	29.35	1.115
Fe IX	188.497	22.36	1.136
Fe IX	197.862	9.51	1.136
Fe X	184.537	78.01	1.136
Fe XI	188.217	101.17	1.125
Fe XI	188.299	78.06	1.125
Fe XII	195.119	121.76	1.106
Si VII	275.361	14.79	1.136
Si X	261.057	15.66	1.136
S X	264.231	15.68	1.115

Note. $F_{\rm scatt}$ indicates the instrument-scattered light flux, and $R_{\rm max}$ is the highest altitude at which the scattered flux is less than 20% of the observed flux (see Section 6.2.2).

O^{7+}/O^{6+} and C^{6+}/C^{5+} to study how the modeled charge states vary with wind speed.

6.2. Emission from the Lower Corona

We use the spectral observations made by the EIS instrument on 2007 November 16. During this time, the EIS $2'' \times 512''$ slit was oriented along the N–S direction and was pointed at seven adjacent positions along the solar E–W direction to cover a total field of view of $14'' \times 512''$ whose center was located at $(0'', 866'')$. The field of view extended from $0.61\,R_\odot$ from the Sun center inside the disk up to a height of $1.15\,R_\odot$ above the limb in the north CH. At each location of the raster, the spectral range covered was $171-211$ Å and $245-291$ Å (with a spectral pixel size of 0.022 Å pixel^{-1}), and the exposure time was 300 s. From the available spectral range, we chose a set of bright and isolated spectral lines (listed in Table 1), which includes as wide a range of charge states belonging to the same element as possible. More details on these observations can be found in Hahn et al. (2010).

6.2.1. Data Reduction and Selection

The data were reduced using the standard EIS software made available by the EIS team through the SolarSoft IDL package (Freeland & Handy 1998). Each original frame was flat-fielded, the dark current and CCD bias were subtracted, the cosmic-ray hits were removed, and the defective pixels were flagged. Residual wavelength-dependent offsets and the tilt of the detectors were also removed. Data were calibrated in wavelength and intensity; the most recent EIS intensity calibration from Warren et al. (2014) was applied. This updated intensity calibration improves the calibration of the long-wavelength channel (246–292 Å) and also allows us to account for the degradation that occurred during the EIS mission. The accuracy of the calibration is $\approx 25\%$.

In order to increase the signal-to-noise ratio, the data were averaged along the E–W direction and re-binned along the slit direction (N–S) in bins of $0.01\,R_\odot$. Only 14 bins extending from 1.025 to $1.155\,R_\odot$ above the limb were used for comparison with the model. Pixels between 1.00 and $1.025\,R_\odot$ were excluded since they might be affected by limb brightening and spicule material (Hahn et al. 2010). The portion of the slit pointed inside the solar disk was only used

for evaluating the instrument-scattered light, as we describe in Section 6.2.2.

Spectral line profiles were fitted with a Gaussian curve removing a linear background. At a certain height above the limb the line emission becomes too weak, and a clear Gaussian cannot be discerned; these measurement are omitted from the analysis. The overall uncertainty in the line fluxes is obtained by taking into account the calibration error, the fitting error in the Gaussian, and the statistical error in the measurement itself.

6.2.2. Scattered Light Evaluation

The EIS optics causes the instrument to scatter the radiation coming from the solar disk into the detector, which can contaminate the observations even in the off-limb section of the slit. This contribution depends on the specific configuration of the instrument and on its pointing at the time of the observations, and it cannot be removed a priori. Landi (2007) devised a method to estimate the contribution of scattered light to coronal emission lines using concurrent observations of chromospheric lines or continuum emission. The presence of emission from chromospheric lines in off-limb observations is only due to scattered light, and its rate of decrease with height can be used to estimate its contribution to the total measured emission. In the case of the EIS spectrometer there is no continuum emission available. The only chromospheric line is from He II. Hahn et al. (2012) showed that the emission by this line in the off-limb section is actually real coronal emission, so this line cannot be used. EIS measured some transition region lines from O IV and O V that can potentially be used, but they are too weak. Instead, we evaluate the scattered light contribution based on EIS observations performed during a partial lunar eclipse, in which the EIS slit pointed at the partially occulted solar disk. Using the flux ratio from the occulted and non-occulted portions of the slit, the EIS scattered light was found to be around 2% of the disk emission (Ugarte Urra 2010, EIS Software Note No. 12).

We evaluate the scattered light flux for each of the lines in Table 1 by averaging their emission in the portion of the slit that covered the disk in the $0.61-0.97\,R_\odot$ range. The scattered light intensity is then taken to be 2% of the average value. The actual scattered light should decrease with distance from the solar disk. By taking a constant 2% value at all distances, we are effectively overestimating the scattered light contribution. This conservative approach ensures that we do not interpret scattered light originating in other features as real emission from the off-limb region. The line intensities over the EIS field of view from $0.93\,R_\odot$ to the northern end of the slit are shown in Figure 2. For clarity of presentation, the Si X intensity is multiplied by 10, S X by 12, and Fe XI 188.2 by 0.6. It can be seen that the intensity drops sharply in the off-limb portion of the slit for the lines belonging to the lower ionization stages. This is consistent with having a small contribution from scattered light; in fact, the local coronal emission, which is proportional to N_e^2, decreases very rapidly with height from the limb, while scattered light usually decreases very slowly. The scattered light levels for each line are shown as dashed horizontal lines, and their values are reported in the third column of Table 1. These values should be taken as estimated upper limits, while the actual contribution is probably lower; in the present observations only part of the slit pointed into the solar disk, and therefore the telescope is less illuminated by the disk compared to the observations used to estimate the
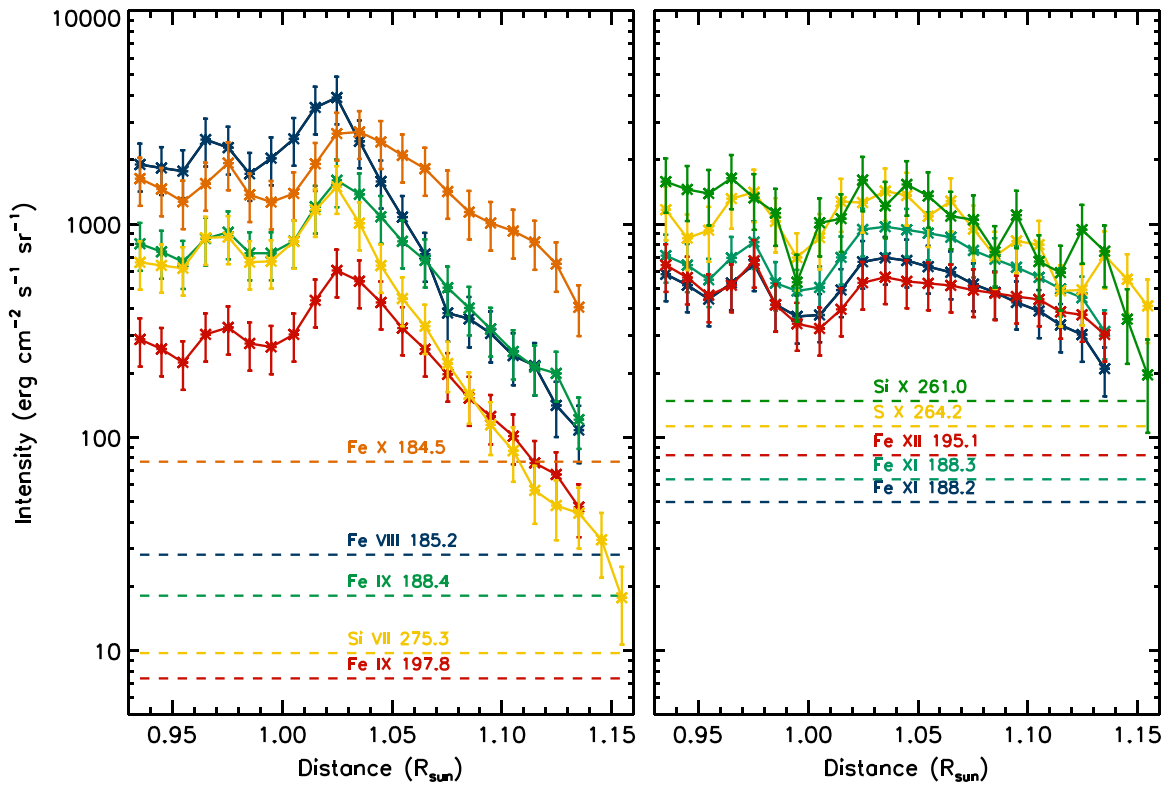
Figure 2. Intensity vs. distance for the spectral lines in Table 1, over the EIS field of view between 0.93 $R_\odot$ and the farthest end of the slit at 1.16 $R_\odot$ (solid curves). The dashed lines show the estimated scattered light intensity for each line. The observed intensities and the scattered light level are color-coded in the same way. For clarity of presentation, the Si x intensity is multiplied by 10, S x by 12, and Fe xi 188.2 by 0.6.

scattered light levels. To exclude any significant contamination by scattered light from this analysis, we conservatively use only observations where the estimated scattered light level is less than 20% of the observed flux. The maximum heights at which this occurs for each of the lines, R_{max}, are reported in the last column of Table 1.

7. RESULTS

7.1. Solar Wind: Frozen-in Charge States

The AWSoM-MIC frozen-in ratios from the field lines described in Section 4 are compared to *Ulysses* observations in Figure 3. The top and bottom panels show the comparison for O^{7+}/O^{6+} and C^{6+}/C^{5+}, respectively, plotted against heliographic latitude. The left column shows the *Ulysses* observations, where the gray curve shows the original data at 3 hr resolution, and the red curve is a moving average over a window of 6 days. The right column shows the corresponding AWSoM-MIC results for the case of a single-temperature electron population. The first thing of note is that the predicted charge state ratios in the region around the equatorial plane are higher than those outside this region, in line with observations. This region corresponds to the location of the slow wind, as can be seen in Figure 4, which shows the modeled (red curve) and measured (blue curve) speeds versus latitude. The overall magnitude of the modeled O^{7+}/O^{6+} and C^{6+}/C^{5+} ratios is about an order of magnitude lower than the observed values at all latitudes. However, the qualitative behavior is markedly similar. The modeled charge states exhibit the well-known behavior of higher charge state ratios at low latitudes around

the heliospheric current sheet, compared to lower (by about an order of magnitude) charge state ratios at high latitudes associated with polar CHs (von Steiger et al. 2000).

Both ratios exhibit larger fluctuations when measured in the slow wind. This behavior cannot be addressed by our steady-state simulation, which cannot describe fluctuations anywhere. On larger timescales, the observations exhibit mid-scale variations on top of the overall variation between the fast and the slow wind. Similar behavior is seen in the model; however, as explained in Section 4, a simulation of a single CR can only be regarded as a "snapshot" taken during *Ulysses*'s polar scan, and the mid-scale variations seen in the model should not be directly compared to specific structures seen in the observations.

These results demonstrate that fast and slow solar wind streams flowing along static open magnetic field lines can carry distinctly different frozen-in charge states. This result will be discussed in detail in Section 8. The overall level of ionization we found in the simulation is too low at all latitudes. From Equation (1) we can see that insufficient ionization rates can be due to several factors: (1) the AWSoM electron density is too low, inhibiting the collisions necessary for ionization to the higher charge states (C^{6+} and O^{7+}), or (2) predicted ionization rate coefficients are too small (which implies that the thermal energy of the electrons is not predicted correctly), or (3) the ion flow speed below the freeze-in height is not predicted correctly, changing the time the different ions spend at each height, and preventing sufficient ionization from occurring. We will explore these factors separately.
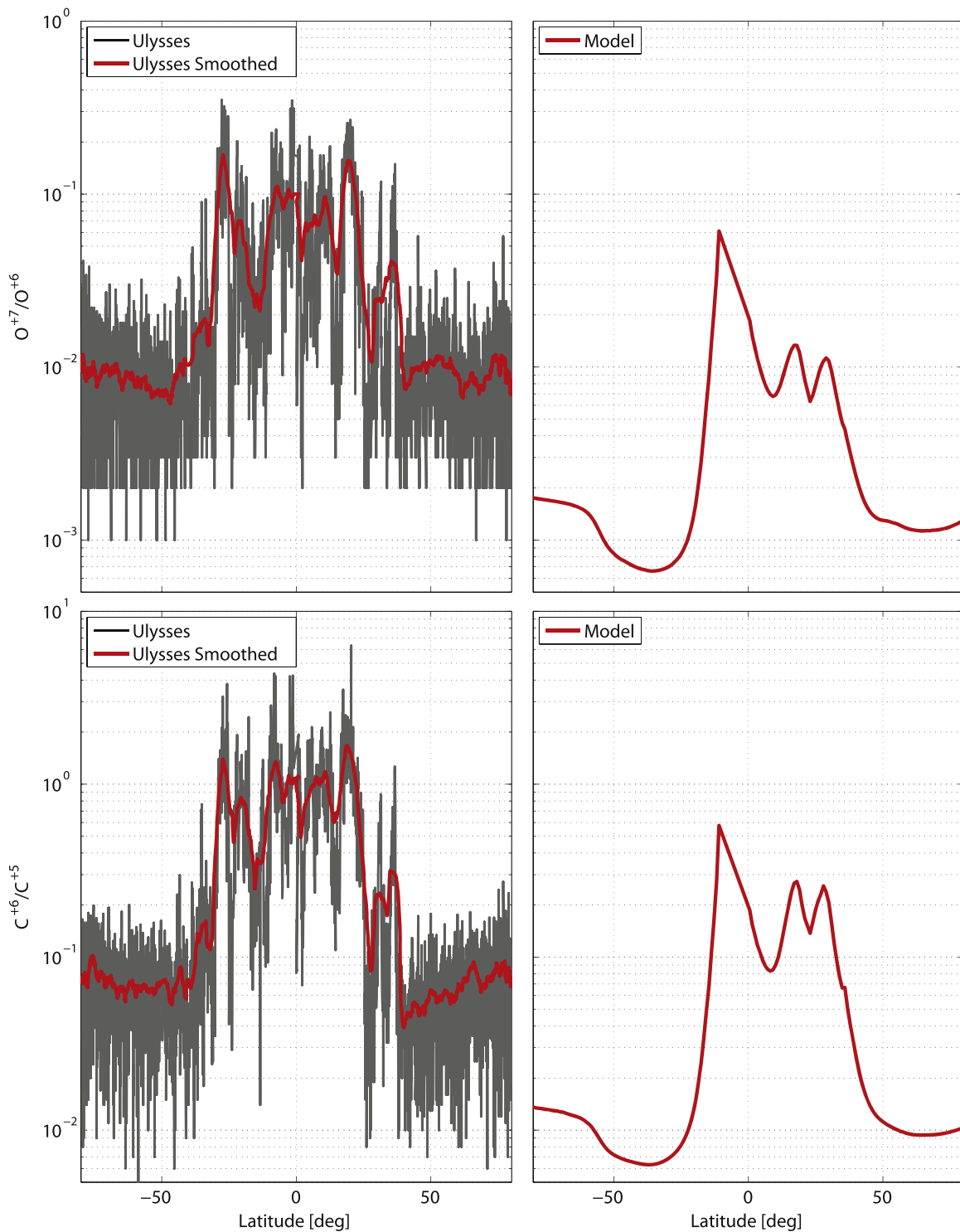
Figure 3. Model-observation comparison of charge state ratios vs. heliographic latitude. The top and bottom panels show the comparison for O^{+7}/O^{+6} and C^{6+}/C^{5+}, respectively. Left: the gray curve shows *Ulysses* measurements taken at 3 hr intervals. The red curve shows the same data smoothed over a 6 day window. Right: ratios predicted by AWSoM-MIC for the field lines described in Section 4, plotted against the latitude reached by the field line at 1.8 AU.

7.1.1. Modeled Electron Density and Temperature as a Cause of Underpredicted Charge States

The coronal electron temperature and density predicted by the present simulation for CR2063 were validated in Oran et al. (2013) using two sets of observations. First, they showed that the 3D thermal structure predicted for CR2063 leads to

synthetic full-disk images in the EUV and soft X-ray range (emitted by the lower corona) that are consistent with observations. Even though the discrepancy between the synthetic and observed full-disk images is larger at certain localized regions (especially around active regions), the large-scale structure is well reproduced. Second, the authors found that the modeled electron density and temperature at the center
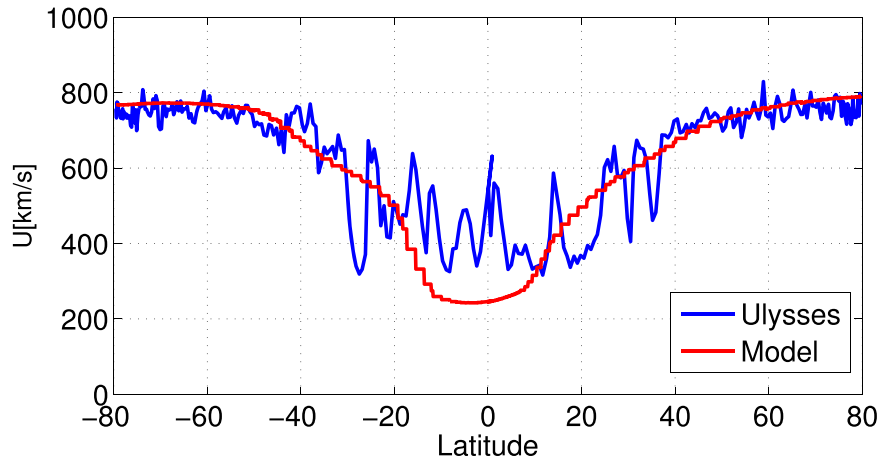
Figure 4. Wind speed vs. heliographic latitude. The blue curve shows *Ulysses* measurements. The red curve shows the AWSoM result.

of the north polar CH were in good agreement with spectroscopic measurements extending from 1.05 to 1.13 $R_\odot$ above the limb.

However, determining the electron density and temperature from remote observations is inherently complicated by LOS effects, since the emission from different regions contributes to the measured intensity. Frazin et al. (2005, 2009) and Vásquez et al. (2010) have developed a tomographic method to reconstruct the 3D thermal structure of the lower corona. The technique, dubbed differential emission measure tomography (DEMT), uses multi-wavelength EUV images of the lower corona taken from different points of view in order to reconstruct the electron density and temperature that are responsible for the emission. If a single observatory is used, the images are collected over an entire solar rotation, until a full coverage of the corona is achieved. For this reason DEMT can only recover steady structures; in regions where the magnetic topology or thermodynamic properties vary significantly during the rotation, the tomographic method fails to reconstruct a single set of thermal properties. These regions are excluded from the analysis. However, the global, large-scale distribution can be reliably recovered. In DEMT, the inner corona (1.02–1.20 $R_\odot$) is discretized on a regular spherical grid, with voxels having a radial size of 0.01 $R_\odot$ and angular size of 2°, in both the latitudinal and azimuthal directions. The tomographic 3D reconstruction of the EUV filter band emissivity in each band (Frazin et al. 2009) allows us to derive the local differential emission measure (LDEM) in each voxel, which describes the distribution of temperatures of the plasma contained in that voxel. By taking moments of the LDEM, the final products of DEMT are 3D maps of the electron density, N_e, and the average electron temperature $\langle T_e \rangle$ in each voxel of the tomographic grid.

We performed a DEMT reconstruction for CR2063 using full-disk images taken at three wavelengths by the Extreme Ultraviolet Imager (EUVI) on board the two *STEREO* spacecraft (Howard et al. 2008). Figure 5 shows how the model compares to the reconstructed electron temperature and density. The data are plotted as longitude-latitude maps over a spherical surface extracted at $r = 1.075\ R_\odot$. The top two panels show the comparison of modeled and tomographic electron temperature, while the bottom pair shows the same comparison for electron density. White regions in the tomographic maps correspond to regions where the tomography method fails,

which occurs mostly around regions with high variability. The black curves show the boundary of the polar CHs based on the magnetic field from AWSoM. The mid-latitude regions, where the temperature and density are much higher, correspond to the closed field streamer belt.

The modeled CH boundaries follow the contours of the streamer belt in the tomography very closely, with small (up to 2°–3°) departures at certain regions. The open-closed boundary of the magnetic field is only plotted for polar CHs, but other closed field regions appear as islands of higher density and temperature outside the main streamer belt, while low-latitude CHs, having lower temperatures and densities, can be seen inside the main streamer belt. These regions have similar sizes and locations in both the model and the tomography. This comparison suggests that the magnetic field topology derived from the MHD solution at this height is realistic. Some discrepancies between the shapes of the CH boundary in the model and the tomographic density structure may be attributed to the fact that both the synoptic magnetogram, used as a boundary condition to the model, and the tomographic reconstruction were obtained from observations taken over the entire CR, and small-scale and dynamic features will not necessarily be captured by either of these methods.

While the modeled electron temperature is in very good agreement with the reconstructed values, the density comparison shows larger discrepancies, with the modeled density about 1.4 times larger than the reconstructed density in the closed field region, and about a factor of 2 lower than the reconstructed density in CHs.

This underprediction of the electron density in CH is also present at larger heights. Using the Fe VIII line intensity ratios observed by EIS during CR2063, Oran et al. (2013) measured the electron density along the center of the north CH, at heights between 1.02 and 1.13 $R_\odot$ above the limb, and compared them to model results (see Figure 13 therein). To make the comparison more quantitative, we calculate the ratio of modeled to measured density using the same data as in Oran et al. (2013). Figure 6 shows the ratio plotted against radial distance. The error bars are due to the uncertainty in the density measurements. Given these uncertainties, it is clear that the modeled values are within the uncertainties in the measurement at most heights. We note that the model/measured ratio is centered around 0.5 at heights $r > 1.04\ R_\odot$, consistent with the model-tomography comparison.
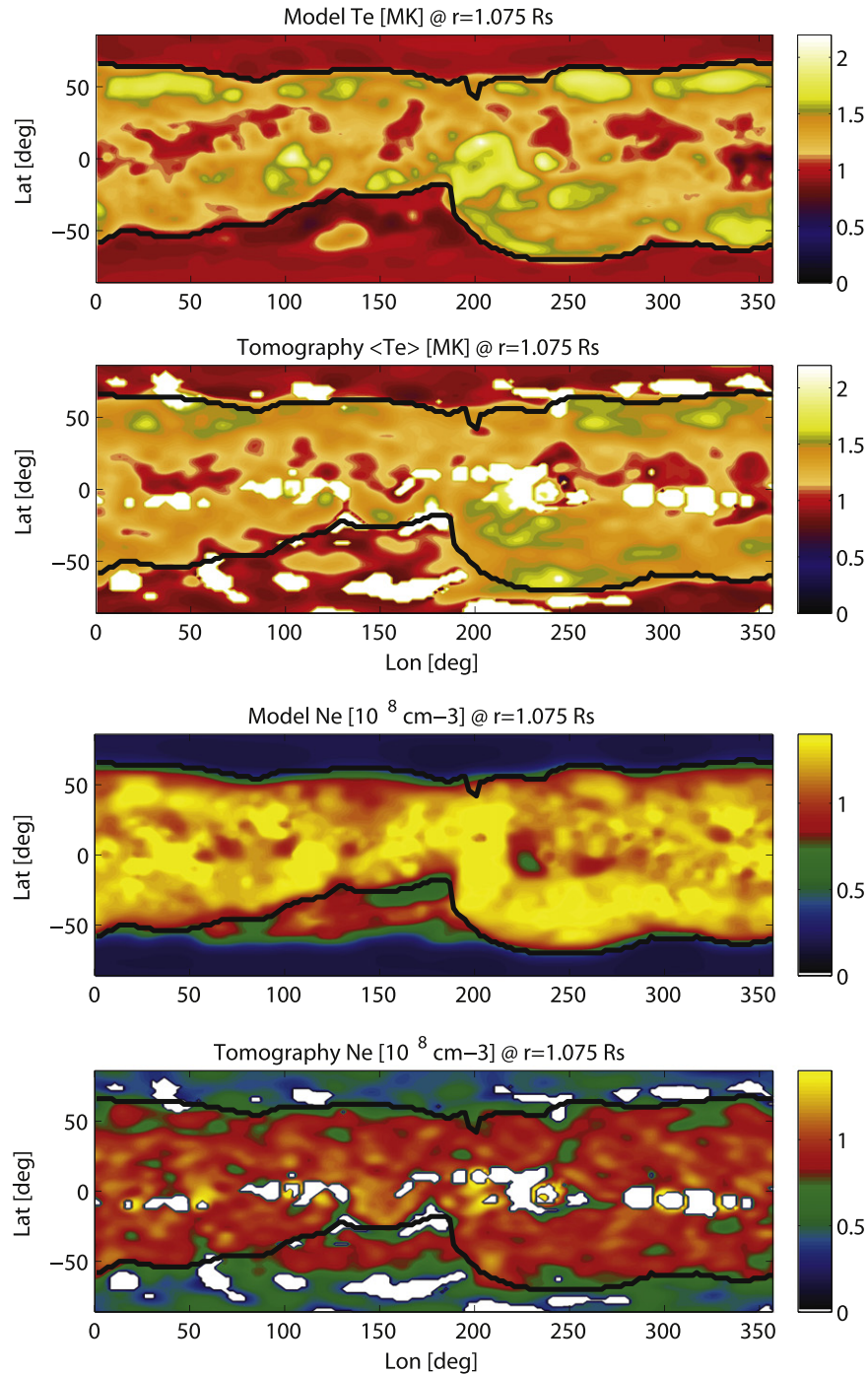
Figure 5. Model and DEMT maps for CR2063 extracted at a height of 1.075 $R_\odot$. Top two panels: AWSoM electron temperature T_e and average electron temperature $\langle T_e \rangle$ from DEMT. Bottom two panels: AWSoM electron density and DEMT electron density. Black curves show the polar CH boundaries extracted from the AWSoM solution. The white regions in the tomographic maps correspond to regions that could not be reconstructed by DEMT.

The lower density predicted by AWSoM in the polar CHs would in general lead to lower collisions rate and therefore to lower ionization. However, it is not immediately clear by how much an electron density that is a factor 2 too low would contribute to the underprediction of the frozen-in values in Figure 3, which are about an order of magnitude too low at all latitudes. To make a quantitative estimation, we repeated the charge state calculation for a few representative field lines, while multiplying the AWSoM electron density by a factor of 2 at all points. We found that the resulting frozen-in values

increase by about a factor of 2. We conclude that the modeled electron density alone is not responsible for the difference between *Ulysses* and AWSoM-MIC charge state ratios.

7.1.2. Impact of Supra-thermal Electrons on the Ionization Rate Coefficients

A second cause of underpredicted charge states is ionization rate coefficients that are too low. The rate coefficients depend on the thermal energy of the electrons. In solving Equation (3), we assumed that the electron possesses a Maxwellian
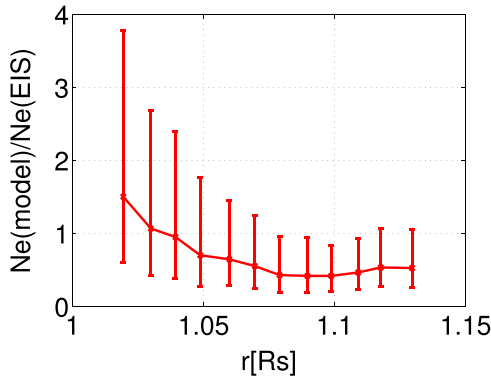
Figure 6. Ratio of modeled to measured electron density vs. radial distance along the center of the north CH. The electron density was measured using Fe VIII line intensity ratios measured by EIS.

distribution function and calculated the rate coefficients based on the Maxwellian temperature. However, there could be additional thermal energy present, in the form of a supra-thermal tail of the distribution function. Even a small population of supra-thermal electrons can increase the ionization rate coefficients significantly. We therefore repeat the charge state calculations using ionization and recombination coefficients based on a main electron population obeying a Maxwellian at the modeled electron temperature, as well as an additional supra-thermal electron population, obeying a second Maxwellian at 3MK, which constitutes 2% of the entire electron population. The values we used here to characterize the supra-thermal population were chosen for demonstration purposes only. A more rigorous determination of these parameters requires exploring the parameter space through modeling and comparison to observations and is beyond the scope of the present paper. We note that these values are consistent with those used by previous authors, as discussed in Section 2.2.

The results are shown in Figure 7, with the same layout and color-coding as in Figure 3. The agreement between the observed and predicted charge state ratios is significantly improved compared to the case without supra-thermal electrons. The modeled C^{+6}/C^{+5} ratio is now in good agreement with the observations in both the slow and fast wind. This result is consistent with previous studies (e.g., Esser & Edgar 2000; Laming & Lepri 2007; Cranmer 2014) that showed that supra-thermal electrons can explain the observed charge state ratios in the solar wind. For the modeled O^{+7}/O^{+6} ratio, the addition of supra-thermal electrons allowed us to obtain a good agreement with observations in the slow wind, while in the fast wind this caused the ratio to become about a factor of 2–3 too high (compared to about an order of magnitude too low without the supra-thermal electrons). This suggests that further fine-tuning of the supra-thermal population size and energy is needed, before a truly accurate and acceptable agreement is obtained. This type of parameter search can be assisted by creating synthetic emission using the predicted ions fractions, to be compared with observations of the lower corona, as we present in Section 7.2.

It is important to note that even though the supra-thermal electrons improved the agreement with the overall magnitude of the observed charge state ratios, they play no role in determining the large-scale structure of these observables. In

fact, the highest charge states occur at the same latitudes whether or not supra-thermal electrons are included, and they are increased by the same factor relative to the fast wind values (about one order of magnitude). Therefore, some other mechanism must be responsible for the higher charge states predicted in the slow wind, as will be discussed in detail in Section 8.

7.1.3. Ion Speeds as a Cause of Underpredicted Charge States

A third cause for underpredicted frozen-in charge states may be due to an inaccurate prediction of the ion flow speeds. If the ion speed is so high that its travel time is shorter than the ionization time, the ionization to the higher charge states will be inhibited. There are two possible factors that can lead to ion speeds that are too high in the AWSoM-MIC simulations: either the wind speed itself is too high, or the assumption that all the ions move at the wind speed is wrong. We note here that the terminal wind speed in the model is in good agreement with *Ulysses* observations, especially in the fast wind (see Figure 4). However, it is still possible that the rate of acceleration at lower heights is not predicted correctly, affecting the evolution. This will be discussed further when we examine the charge state distributions in the lower corona in Section 7.2.

Alternatively, heavy ions can move at different speeds with respect to the background plasma, commonly referred to as differential flows. Bürgi and Geiss (1986) showed that heavy elements, including C and O, may have flow speeds that are smaller than the proton speed at $r < 20\,R_\odot$. Ko et al. (1997) showed that if the heavy ions are slower than the wind, higher ionization states are achieved, leading to a better agreement with in situ observations. It is also possible that ions of the same element flow at different speeds with respect to each other. Esser & Edgar (2001) showed that if ions with charge state $m+1$ flow faster than the ions with charge state m, then the recombination of the $m+1$ ions back to the m charge state can be significantly inhibited, resulting in higher ionization compared to a single-speed case. However, the extent at which differential flows occur is not clearly known. One could hope to determine their extent empirically by changing the flow velocities of the different ion species until a good agreement with charge state observations is reached. However, Esser et al. (1998) found that the observed frozen-in charge state distributions could be reproduced by many different flow profiles, making it difficult to make a conclusive determination. Furthermore, the effect of differential flows on the predicted charge states was found to be comparable to the effects of supra-thermal electrons (Ko et al. 1998; Esser & Edgar 2001). In fact, it is possible that both processes take place in the corona, and it is hard to determine their separate contributions. Here, again, the simultaneous comparison to in situ and remote observations of the lower corona could assist in constraining parametric studies.

7.2. Lower Corona: Emission by Heavy Ions in a Polar Coronal Hole

We calculated the synthetic LOS fluxes for all the lines in Table 1 and compared them to their corresponding EIS observations. The magnitude of the synthetic emission from each point along the LOS is proportional to the relative abundance of the ion responsible for the emission, or the ion fraction, $N(X^{+m})/N(X)$, as seen in Equation (4). For each spectral line, we use ion fractions derived from:
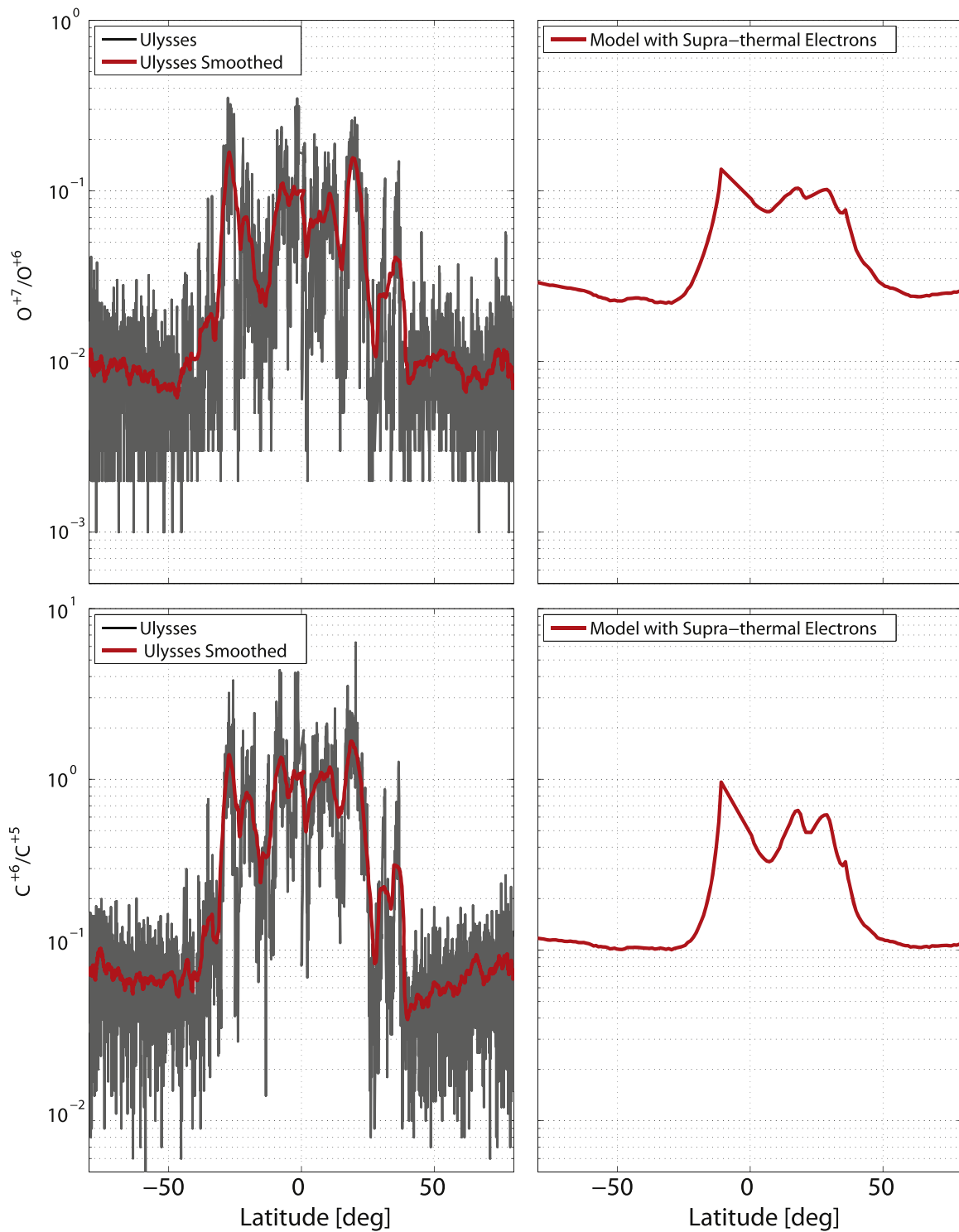
Figure 7. Model-observations comparison of charge state ratios vs. heliographic latitude, as in Figure 3, but for the case where a supra-thermal electron population is added in the MIC simulation.

1. Charge state evolution in a single-temperature electron thermal core population.
2. Ionization equilibrium in a single-temperature electron thermal core population.
3. Charge state evolution assuming an additional supra-thermal electron population.
4. Ionization equilibrium assuming an additional supra-thermal electron population.

Cases 1–2 and cases 3–4 will be based on different ionization and recombination rate coefficients (see Section 2.2). Within each pair, the charge states are either allowed to evolve freely according to Equation (3), or ionization equilibrium is imposed at each point along the trajectory (determined from the steady-state solution of Equation (1)). This will allow us to gauge the extent of departures from equilibrium due to the flow
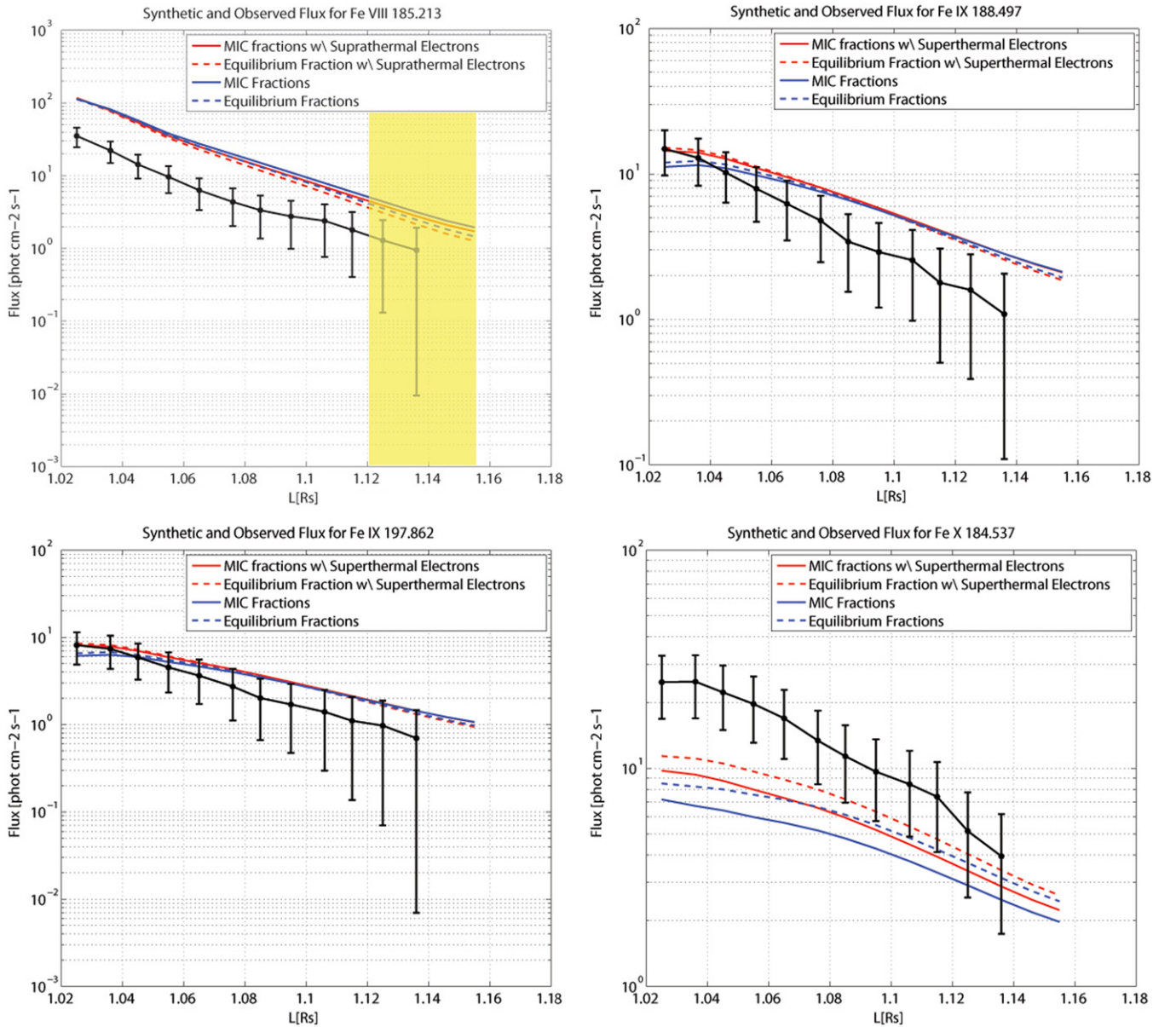
Figure 8. Observed and synthetic LOS flux vs. radial distance for emission lines from Fe VIII to Fe X. The black curve shows EIS observations and their uncertainties. The two blue curves show the synthetic flux for a single-temperature electron population. The two red curves show the synthetic emission including supra-thermal electrons. In each pair, the solid curve was obtained using the MIC ion fractions in the contribution function, while the dashed curves were obtained using ion fractions determined from ionization equilibrium. The shaded area represents heights at which the scattered light may contribute more than 20% to the observed flux.

speed. In what follows, we refer to the evolved charge states as MIC ion fractions. In cases 3–4, which include the supra-thermal electrons, we calculated the synthetic emission using modified level populations, as outlined in Section 2.2.

Figures 8–10 show the comparison of the synthetic and EIS fluxes as a function of height for all the lines. In each figure, the black curve shows the EIS observations and their uncertainties. The two blue curves show the synthetic flux for a single-temperature electron population, while two red curves are for the supra-thermal case. Within each pair, the solid curve is based on MIC ion fraction, while the dashed curve is based on ionization equilibrium fractions. The height ranges shaded in yellow represent the distances at which scattered light contamination may be higher than 20% of the observed flux, taken from Table 1.

7.2.1. Under- and Overpredicted Charge States

There are seven lines covering different charge states of Fe, from 8 to 12. As can be seen, the synthetic emission is overpredicted for charge states 8 and 9, while it is under-predicted for charge states 10–12, for all four types of predicted ion fractions. The best agreement is achieved for the spectral line Fe IX λ197.862, where the synthetic emission is within the uncertainty of the measured flux at most heights.

The fact that the synthetic fluxes are either over- or underpredicted for ions of the same element removes the possibility that the disagreement is due to uncertainties in elemental abundances, as these should shift all the predicted fluxes in the same direction. Another source for the discrepancy could be contamination from hotter streamer material that might cross the LOS, which will preferentially contribute to the
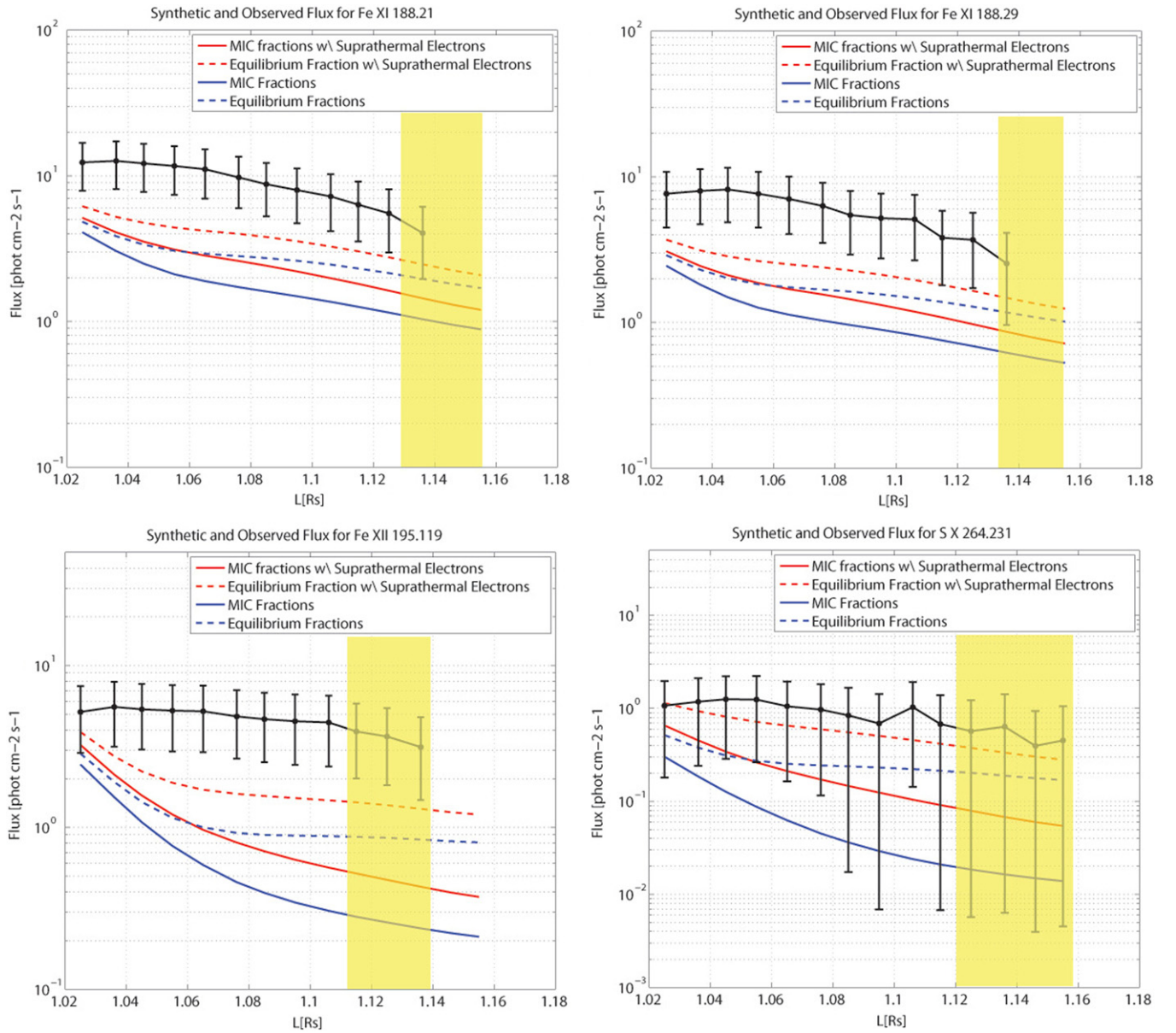
Figure 9. Observed and synthetic LOS flux vs. radial distance for emission lines from Fe XI, Fe XII, and S X. The color-coding is similar to Figure 8.

observed emission from the higher charge states. This contribution is hard to quantify from LOS observations alone; however, the magnetic field configuration obtained by the model shows that no closed field lines cross the LOS. The physical interpretation of these discrepancies is that Fe is not ionized rapidly enough in the model, leading to an over-population (and emission) of low charge states and an insufficient population of high charge states. Landi et al. (2014) found similar behavior when analyzing synthetic emission from several models, including the AWSoM model, for an ideal dipole magnetic field case.

Since Fe only freezes-in around $4\,R_\odot$, the model may still achieve the correct ionization status at altitudes higher than the EIS field of view, and specifically the correct frozen-in charge states. To examine this, we compared the predicted frozen-in value of $\langle Q \rangle_{Fe}$ to the *Ulysses* observations made above the north polar CH, which is the other end of the wind trajectory for most of the plasma observed here by EIS. The results are

shown in Figure 11. The gray curve shows the value of $\langle Q \rangle_{Fe}$ measured by *Ulysses*/SWICS at 3 hr resolution versus latitude. The blue curve shows a moving average over a 6 day window, while the red curve shows the modeled frozen-in values, for the case including supra-thermal electrons. The model results for the case of a single-temperature electron population give only slightly smaller values at these heights (around 0.1–0.2 lower than the supra-thermal case). It can be seen that the modeled $\langle Q \rangle_{Fe}$ is very close to the observed values, and it differs by less than and one charge state from the smoothed values. Recalling that the charge state composition has an uncertainty between 10% and 25%, it is clear that the discrepancy between the model average charge state and the observations at *Ulysses*'s orbit is small compared to that found for the separate charge states in the lower corona; there, the emission from the highest charge state in our data set, Fe XII, is almost an order of magnitude lower than the observations, even with the inclusion of supra-thermal electrons. This may mean that the
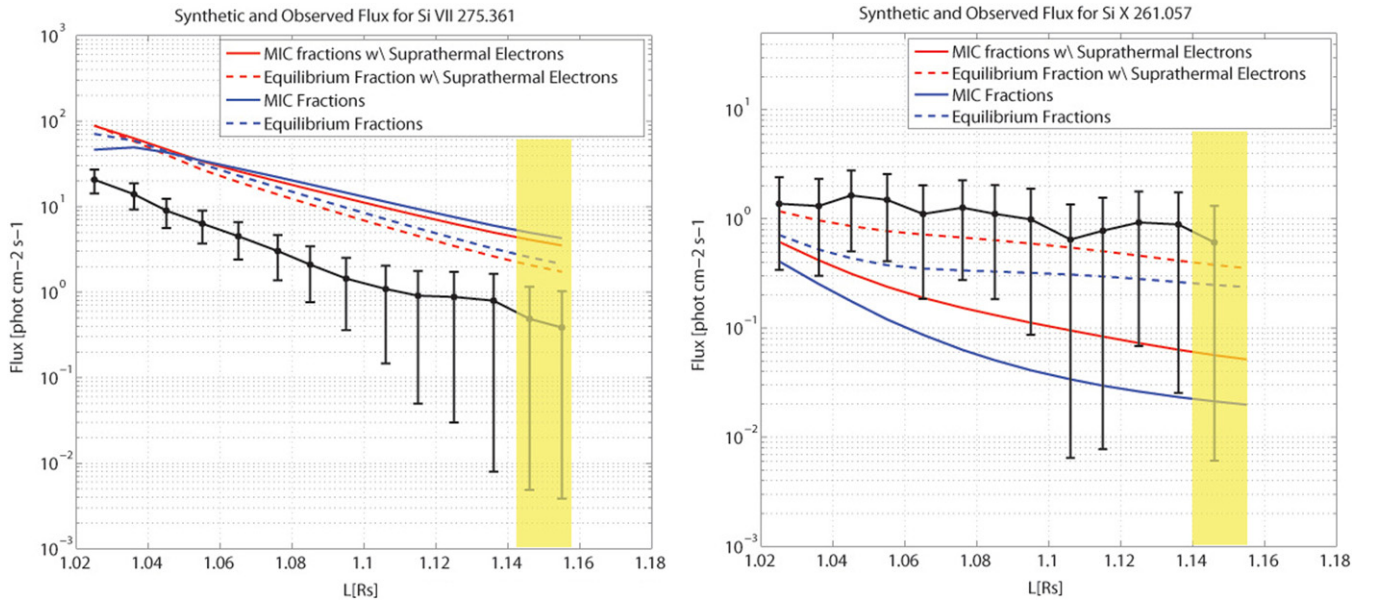
Figure 10. Observed and synthetic LOS flux vs. radial distance for emission lines from Si VII and Si X. The color-coding is similar to Figure 8.
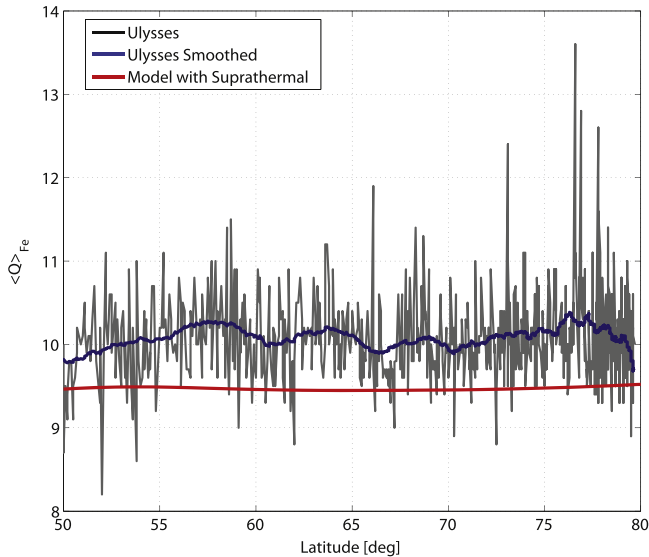

Figure 11. Frozen-in average charge state of Fe plotted vs. heliographic latitude above the north CH. The gray curve shows *Ulysses* measurement taken at 3 hr intervals. The blue curve shows the same data smoothed over a 6 day window. The red curve shows the average charge state predicted by AWSoM-MIC (for the case including supra-thermal electrons).

underpredicted ionization of Fe in the lower corona eventually recovers at larger heights, at least partially, giving rise to frozen-in values closer to observations. However, care must be taken when making this conclusion only from comparing the average charge state. The full charge state distribution may reveal larger discrepancies, especially when considering charge states much larger or smaller than the mean of the distribution. Unfortunately, the entire charge state distributions from SWICS are not publicly available. Thus, the comparison presented here for the modeled and observed values of $\langle Q \rangle_{Fe}$ should be considered as a rough comparison; the heliosphere may be just as underionized as the lower corona.

The same effect of underestimated ionization can be seen in the two lines belonging to Si (Figure 10), where the Si VII line

flux is overpredicted and that from Si X is underpredicted. Unfortunately, there are no publicly available data of Si charge states from *Ulysses* at the time of this publication. Finally, the agreement between the predicted and observed flux for the S X line is very good. However, since only a single line is used here, it cannot reveal further information about the charge state evolution.

7.2.2. Signatures of Supra-thermal Electrons in Line Intensities

In many of the spectral lines the supra-thermal electrons give rise to a noticeable difference in the predicted fluxes, making this type of model prediction a potential diagnostic for the properties of the supra-thermal electrons themselves. In these lines, the inclusion of supra-thermal electrons improved the agreement between predicted and observed values. The fluxes emitted by the low ionization states, which are overpredicted, are smaller in the supra-thermal case, while the reverse occurs for the underpredicted fluxes from the higher charge states. This can be explained by the fact that the supra-thermal electrons increase the ionization rate coefficients; in this case a larger portion of the element is ionized to a higher charge state, leaving fewer ions in the lower charge states. The resulting emission from the low and high charge states decreases or increases, respectively, becoming closer to the observed values for all charge states.

This result, taken in conjunction with the comparison of modeled and observed frozen-in charge states discussed in Section 7.1, demonstrates that supra-thermal electrons below the freeze-in height lead to a better agreement with observations at both ends of the wind trajectory. Furthermore, by calculating the emission assuming a non-Maxwelian electron distribution function, we showed that supra-thermal electrons may have a signature in the line intensities. This suggests that the presence of supra-thermal tails below the freeze-in height may reconcile the discrepancies between the coronal electron temperature derived from spectral observations (which assume a Maxwellian electron population) and the temperature derived from the frozen-in charge states; the supra-thermal population can supply the missing energy required for explaining the

charge states. Further, these results serve as proof of concept that the observed line intensities can potentially be used to gain information about the electron distribution in the lower corona. This is in line with the results obtained by Dzifčáková (2006), who found that electron populations with different κ distributions would give rise to different line intensities and suggested using observed line intensity ratios to diagnose the distribution and determine its κ parameter. A similar technique can be used for supra-thermal electrons obeying a second Maxwellian, as in this work. The parameters of the supra-thermal electrons (i.e., their proportion of the population and their energy) can be empirically adjusted to improve the agreement with observed intensities, using as many lines and from as many instruments as possible. However, the spatial distribution of supra-thermal electrons may not be uniform below the freeze-in height, as pointed out by Laming & Lepri (2007). This introduces additional degrees of freedom in any parametric study aiming to determine the properties of supra-thermal electrons.

7.2.3. Departure from Equilibrium and Wind Acceleration

The synthetic emission calculated using equilibrium ion fractions agrees better with the observations compared to the MIC ion fractions, both with and without supra-thermal electrons. In other words, the model overestimates the departures from equilibrium. This may be explained by ion speeds that are too large, not allowing them sufficient time to achieve a charge state distribution that is closer to the equilibrium for the local conditions. An overpredicted wind speed is also consistent with the overpopulation of the low charge states of Fe and Si, which occur for both ionization equilibrium and fully evolved charge state distributions, as discussed in Section 7.2.1.

As in the case of the in situ charge states, these discrepancies might be resolved if the ions are allowed to have differential flow speeds, in effect changing the ionization rates. Another possibility is that the predicted wind speed is not realistic. We saw that the wind speed at 1–2 AU agrees well with the observations, especially above the CH (see Figure 4); however, it may still be too large below the freeze-in height. If this is the case, then it implies that the wind acceleration process assumed in the model might need to be further refined. In AWSoM the wind is accelerated by gradients in the thermal pressure and the Alfvén wave pressure. In turn, wave pressure gradients are to a large extent created by wave reflection. Consequently, the reflection coefficient will have a large impact on the modeled wind acceleration rate. In the AWSoM simulation used in this work, taken from Oran et al. (2013), the authors assumed a spatially uniform reflection coefficient. In reality, the reflection coefficient depends on the gradients in the Alfvén speed, and thus it will vary with location. Future work will explore these effects using a self-consistent description of the reflection coefficient, such as the one presented in van der Holst et al. (2014).

8. DISCUSSION: THE HIGHLY IONIZED STEADY SLOW WIND

The main result of Section 7.1 is that the observed large-scale variation of the charge state ratios O^{7+}/O^{6+} and C^{6+}/C^{5+} with latitude can be produced by a model where both fast and slow wind comes from CHs and flows along static open magnetic field lines. This is an important result, since the slow

wind charge states often serve as observational support to dynamic release models, in which the source regions of the slow wind are coronal loops, and the acceleration mechanism is driven by intermittent reconnection events. It is therefore worthwhile to understand how the variation in charge states between the steady fast and slow wind is obtained by the model, which is the subject of the present section.

Before we attempt to answer this question, it is important to put this work in context. A steady-state model cannot describe any transient phenomena and thus cannot address the high and sudden fluctuations of the charge states observed in the slow wind; these are probably caused by dynamic release due to reconnection between open and closed field lines (Fisk et al. 1998; Wang et al. 2000; Fisk 2003; Fisk & Zhao 2009; Antiochos et al. 2007, 2011, 2012), as discussed in the Introduction. The AWSoM model also does not include a mechanism for heavy-element fractionation and therefore cannot address the FIP bias found in the slow wind. Thus, our results cannot be used to contradict the dynamic release models. Rather, they offer a complementary picture to slow wind formation, as they demonstrate that a sub-class of slow wind can exist that does not come from coronal loops, and which carries high ionization levels that are already skewed toward the typical values observed in the slow wind, albeit without the fluctuations. If this is indeed the case, this type of slow wind will be relatively steady, will carry high charge states, but most likely will not exhibit an FIP bias, since biased abundances are generally formed in closed field structures (e.g., Feldman & Widing 2003). The relation between this complementary picture and dynamic release models will be discussed in more detail in Section 8.3.

8.1. The Source Region of the Steady Slow Wind

The latitudinal variation of the frozen-in charge state ratios seen in the AWSoM-MIC results suggests that the open field lines carrying the fast and slow wind undergo different evolution below the freeze-in height. In order to characterize these differences and locate the source regions of the different wind types, we examine the evolution of the charge states and wind properties close to the Sun. We choose a new set of open field lines with footpoint locations ranging from the poles toward the streamer belt, in both hemispheres. These are shown as the blue curves in the top panel of Figure 12. The solar surface is colored by the electron density, while thick purple lines show additional open and closed field lines, representing the overall structure of the corona. To make the analysis simple, we selected field lines that are rooted close together in longitude, so that the conditions encountered by adjacent field lines will vary smoothly. The mean longitudes of the footpoints in the northern and southern hemispheres are different, due to the shape of the streamer belt separating the two groups. For the northern hemisphere group, the open field lines belong to three different structures, from north to south: a polar CH, a pseudo-streamer, and a low-latitude CH just below it. For the south hemisphere, the selected field lines come mostly from inside the polar CH, but their footpoints extend into lower latitudes than the north hemisphere group, where they straddle the boundary of the helmet streamer from the left.

The bottom panel of Figure 12 shows the same blue field lines shown in the top panel, flattened onto one plane for clarity, where the vertical and horizontal axes represent the distance from the equator and the distance from the polar axis,
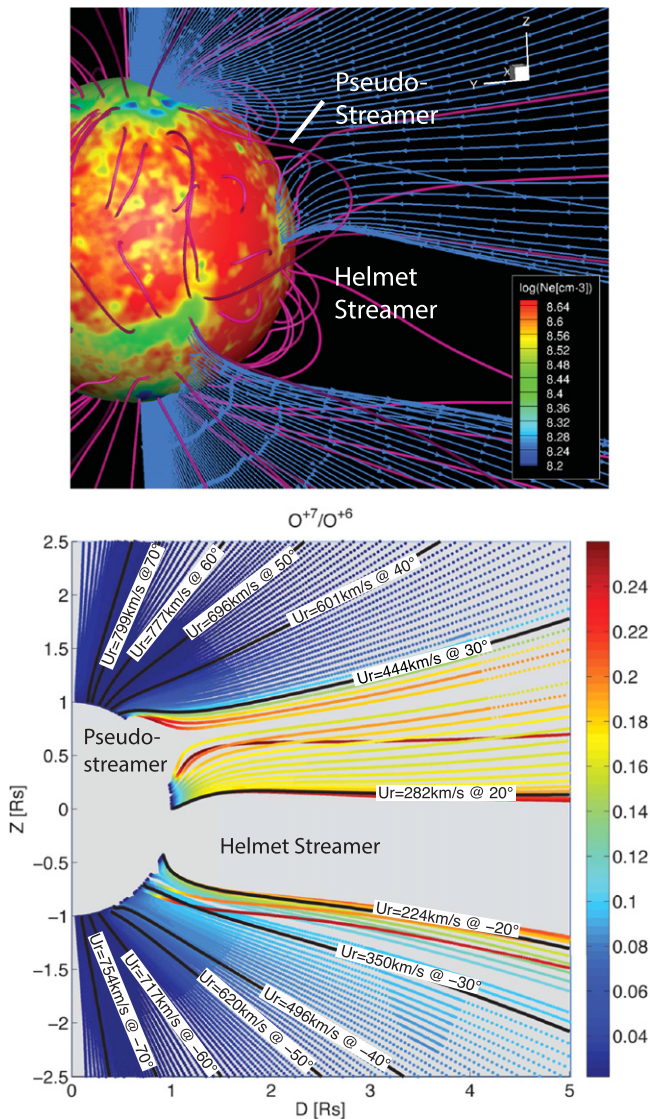
Figure 12. Top: AWSoM solution for CR2063. The solar surface is colored by the electron density. Blue curves show open magnetic field lines for which the charge state evolution is analyzed in Section 8.1. Purple curves show selected open and closed magnetic field lines. Bottom: predicted O^{7+}/O^{6+} ratio along the blue field lines shown in the top panel, presented in one plane. The field lines are colored by the local charge state ratio. Black field lines are those reaching 1.8 AU at $10°$ spacing in latitude. The labels show the wind speed and latitude at 1.8 AU of the respective line.

respectively, of each point along each field line. The field lines are colored by the magnitude of O^{7+}/O^{6+} predicted by an AWSoM-MIC simulation with supra-thermal electrons. The labeled black field lines demonstrate how the magnetic field in the corona maps to the heliosphere: the ends of these field lines intersect a spherical surface at 1.8 AU at $10°$ spacings. The labels show the wind radial speed and the heliographic latitude at that distance. The regions covered by the helmet streamer and the pseudo-streamer are also labeled. Note that the range of latitudes without open field lines only reflects the structure close to the Sun; out in the heliosphere, these latitudes will be filled by field lines rooted in other longitudes on the solar surface.

The distribution of O^{7+}/O^{6+} in Figure 12 shows that the highest charge state ratios (~ 0.2) originate from the pseudo-

streamer and the low-latitude CH just below it and are carried by a slow wind. Charge state ratios of ~ 0.1 originate from the edges of the polar CHs and are also carried by slow wind flows (up to $450\,km\,s^{-1}$). These field lines reach latitudes of up to $\pm 40°$ at 1.8 AU. In contrast, the fast wind ($>600\,km\,s^{-1}$) comes from deeper inside the polar holes and carries charge state ratios between 0.02 and 0.08, smoothly increasing from the center of the hole toward lower latitudes. These values are consistent with those used by Zurbuchen (2001) to distinguish between fast and slow wind streams in in situ observations taken during solar minimum. Using *Ulysses* and *ACE* data, they found that the slow wind exhibited ratios at and above 0.1, while values of $O^{7+}/O^{6+} < 0.1$ were associated with fast wind streams coming from polar CHs. Zurbuchen et al. (2002) found that the polar fast streams can carry O^{7+}/O^{6+} lower than 0.02, which is similar to the lower limit of the frozen-in O^{7+}/O^{6+} ratio we found in simulating this specific set of field lines.

The connection we made in Figure 12 between the wind at 1.8 AU and the corona reveals three source regions of highly ionized slow wind streams: pseudo-streamers, low-latitude CHs, and the boundaries of polar CHs. The latter was suggested to be the source region of the slow wind by several authors, who related the low speeds to the larger expansion of the open flux tubes rooted in this region (Suess 1979; Kovalenko 1981; Withbroe 1988; Wang & Sheeley 1990; Cranmer & van Ballegooijen 2005). Cranmer et al. (2007) and Cranmer (2014) calculated the charge state evolution of O ions in an axially symmetric solar model driven by turbulent waves. Their model prescribed an idealized magnetic field topology of expanding flux tubes, where the expansion factor increased from the center of the CH toward the streamer leg. They found that the resulting frozen-in charge state ratio O^{7+}/O^{6+} increases with decreasing wind speed, which is in qualitative agreement with the observations. A very good agreement was achieved in the case of an electron κ distribution with $\kappa = 10$ (see Figure 3 in Cranmer 2014). However, inside the fast wind, their predicted charge state ratio exhibits a sharp increase when moving from wind speeds of ~ 650 toward $\sim 750\,km\,s^{-1}$ (i.e., toward the center of the CH). The magnitude of this increase is smaller in the updated calculation of Cranmer (2014), and it is comparable to the size of the variations in the observed O^{7+}/O^{6+} ratio. Here we have directly simulated the charge state evolution at all latitudes using a realistic magnetic configuration and verified that the observed charge state ratios can be reproduced with values that are in agreement with observations, at least in their large-scale behavior.

In summary, in the AWSoM-MIC simulations, the coronal hole boundaries (CHBs) form the low-latitude slow wind, which carries charge states of about 0.1 for the case of O^{7+}/O^{6+}, while other open field regions such as the pseudo-streamer supply an even higher charge state ratio (around 0.2). Thus, our simulations show that the steady-state model can not only produce higher charge states in the slow wind but also account for some of their variations within the slow wind, which can be linked to the magnetic topology of the corona. This is a distinct capability of a global model that is constrained by the observed magnetic field.

8.2. How and Why Are the High Charge States Formed?

The ionization status of a given element at a given location along a field line depends on the wind conditions along its path up to that point. As is clear from Equation (1), the properties
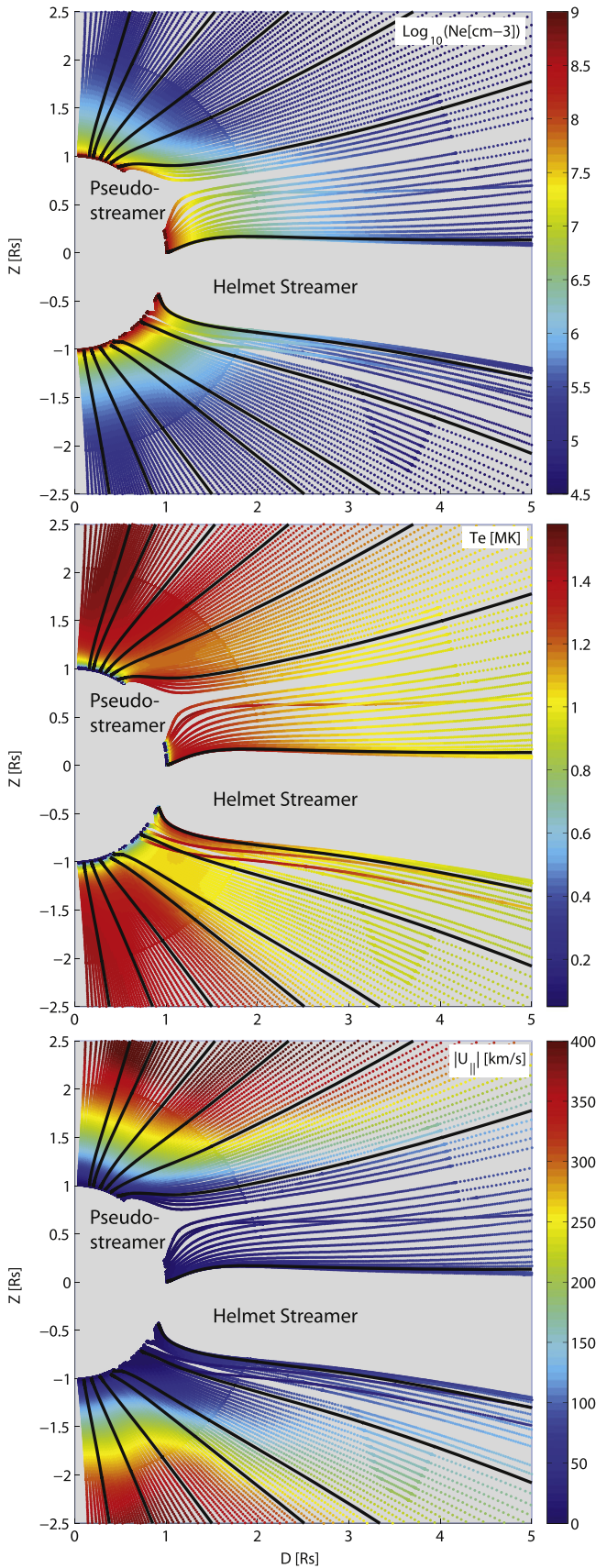
Figure 13. AWSoM solution for CR2063, along the blue field lines in the left panel of Figure 12. From top to bottom: electron density, electron temperature, and speed parallel to the field line. Black curves are the same as in the right panel of Figure 12.

that control the evolution are the electron density and temperature and the wind speed. These quantities are plotted in Figure 13, along the same field lines as in Figure 12. The black field lines are identical to those plotted in Figure 12, but their labels were removed for clarity. The top panel shows the electron density, the middle panel shows the electron temperature, while the bottom panel shows the wind speed.

In the previous section, we identified the polar CHB regions as the source region of a large part of the slow and highly ionized wind. The field lines belonging to the CHBs in Figure 13 exhibit higher electron densities at their base and a slower fall-off of density with radial distance, compared to lines coming from deeper inside the CHs (top panel). Examining the electron temperature (middle panel), we can see that the largest temperatures near the footpoints occur very close to the streamer leg. The higher densities in the CHB (as well as in the pseudo-streamer and the low-latitude CHs) also lead to lower wind speeds (bottom panel) due to conservation of mass flux. Thus, the CHBs are characterized by higher electron density, higher electron temperature, and slower wind speed compared to deeper in the CH at any given height. The higher density and temperature would lead to higher ionization rates, which are proportional to the electron density and increase with increasing incident electron energy. Furthermore, due to the lower speeds, the CHB wind will spend more time in the collisional environment close to the Sun, allowing for more ionization to occur. All these factors combine to produce an overall higher ionization and higher frozen-in charge states.

It is interesting to note that the electron temperature above the poles, which are the source region of the fast wind, can be almost as high as that reached along CHB field lines. Despite this fact, the fast wind does not get ionized to similar levels to the slow wind. This is because the density falls off faster in the fast wind, inhibiting collisions with electrons and causing the charge states to freeze-in before they reach the higher-temperature regions along their trajectory. This points to an important limitation of methods that infer coronal temperatures from in situ charge state observations: if the density is low enough in the lower corona, the frozen-in charge states will not carry information about higher temperatures that may be reached above the freeze-in height.

8.3. The Steady Wind from CHBs as a Subset of the Non-steady Slow Wind

The picture presented here of the formation of a steady and highly ionized slow wind complements dynamic release models as follows. The *Ulysses* observations show that the mean level of charge state ratios is higher in the slow wind than in the fast wind (see, for example, the smoothed curve in Figure 7). Furthermore, charge state ratios as low as those found in the fast wind are rarely present in the slow wind observations covered in this data set. This pronounced increase in charge states is consistent with a scenario where the observed non-steady slow wind is in fact a mixture of material from closed field regions and material from the open field lines from the polar CHBs and low-latitude CHs, which already carry charge state ratios that are higher than those observed in the fast wind. Thus, it is possible that the slow wind simulated by the steady-state model can be a constituent of the variable non-steady slow wind. In this case, this subset of slow wind will be steady and will carry intermediate to high charge states. Since it does not originate from closed magnetic structures, we can expect this subset of slow wind to have non FIP-biased

elemental abundances. We note, however, that the elemental abundances may differ between slow and fast wind streams even in the scenario of a steady wind flowing along open field lines, as discussed in Cranmer et al. (2007).

This sub-set of the slow wind has been possibly identified in *Ulysses*/SWICS measurements of the solar wind in Stakhiv et al. (2015), which found highly ionized wind streams exhibiting photospheric abundances. The future *Solar Orbiter* mission may allow us to further examine whether this wind can be detected in observations. This mission, due to launch on 2016 January, will approach the Sun at distances as close as 0.28 AU. The Heavy Ion Sensor, which is part of the Solar Wind Analyzer on board *Solar Orbiter* (Solar Orbiter Definition Study Report, 2011), will be able to measure the ionic charge states and abundances of key elements, offering a new window into the state of the solar wind before it is modified by its propagation through the complex structure of the heliosphere.

8.4. Enhanced Electron Density and Temperature at the Source Region

The formation of the highly ionized steady slow wind in the AWSoM-MIC simulations is explained by the fact that the electron density and temperature are higher and the wind speed is lower at the slow wind source regions compared to those found in the source region of the fast wind (see Section 8.2). For the picture to be valid, these properties of the source region of the slow wind have to be confirmed observationally and, if possible, explained theoretically. Further, if the electron density and temperature enhancements are indeed responsible for the formation of the highly ionized steady slow wind, then they should be present globally, and not only in the set of field lines we analyzed in Sections 8.1 and 8.2. Since most of the slow wind comes from the polar CHBs, we will focus on these regions and defer the analysis of the more complex low-latitude CHs and pseudo-streamers to a separate study.

8.4.1. Observational Evidence Using EUV Tomographic Reconstruction

We use the tomographic reconstruction of CR2063 presented in Section 7.1.1 to determine whether the CHB region exhibits the higher densities and temperatures predicted by AWSoM. It is hard to discern these properties just by inspecting the tomographic maps in Figure 5. For a clear quantitative examination, we calculate the average variation of density with latitude over the entire polar CHs. For each longitude in the model and tomographic maps in Figure 5, we extract the electron density as a function of angular distance (in latitude), measured from the edge of the streamer belt toward the pole. Here we define the edge of the streamer using the first open field lines found in the model, whose locations appear as the black curves in the maps. For each angular distance, the densities from all longitudes are averaged together. A box in the longitude range of [50, 260] and latitude [−90, 30] was excluded from the analysis, since this region exhibits a large extension of the CH into lower latitudes, embedded with several islands of closed field regions. The results are shown in Figure 14 for the north and south CHs. The black curve in each plot shows the density profile extracted from the tomography, while the red curve shows that extracted from the modeled density map. The error bars represent the standard deviation
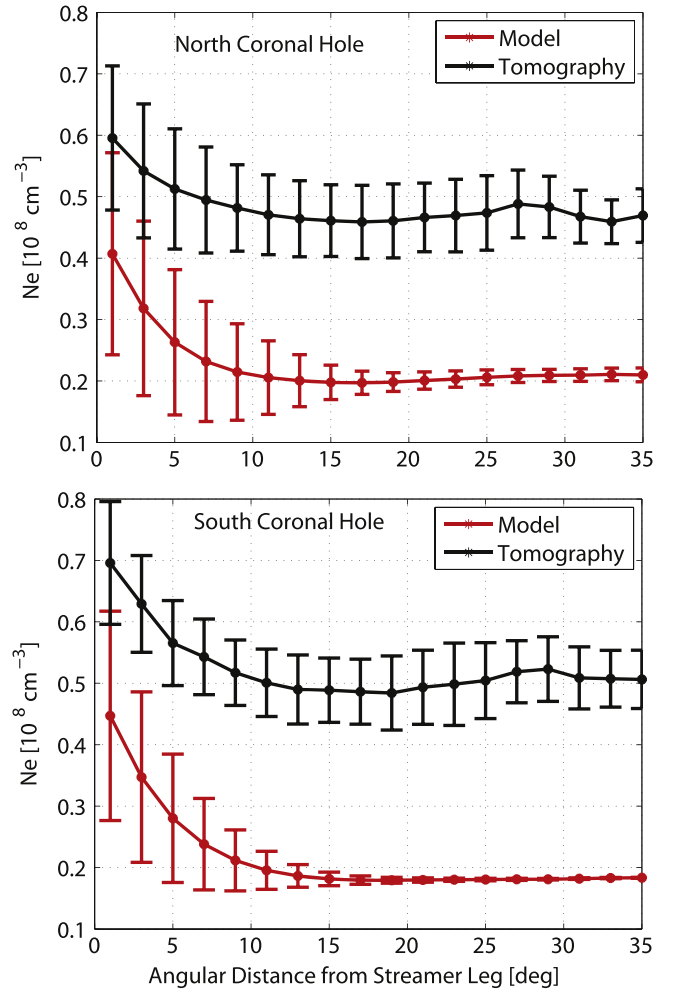

Figure 14. Electron density vs. angular distance in the north (top) and south (bottom) coronal holes for CR2063, extracted from the model and tomography density maps at $r = 1.075\ R_\odot$. Angular distance is measured from the streamer leg (0°) toward the pole (30°). The density is averaged over all longitudes. The black and red curves show data extracted from tomography and the model, respectively. Error bars show the standard deviation from the averaged values taken from all longitudes.

from the average over longitude. The modeled density is lower than the reconstructed density, by a factor of 2–3, which is expected since this discrepancy exists in the maps. However, two important features emerge in both the model and the tomography averages:

1. The density is highest at the edge of the CH and smoothly decreases until it reaches an almost constant value by 10°–15° away from the outer edge.
2. The rate of decrease versus angular distance is similar in both the model and the tomography.

Our finding that the electron density inside CHs varies with latitude may seem to be in contradiction with other observational determinations. Guhathakurta & Holzer (1994) used white-light coronagraph images to determine the electron density in polar CHs and concluded that it does not vary with latitude. However, their definition of a CH somewhat differs from the one used here, strictly referring to regions exhibiting flat polarization brightness (pB) profiles with respect to
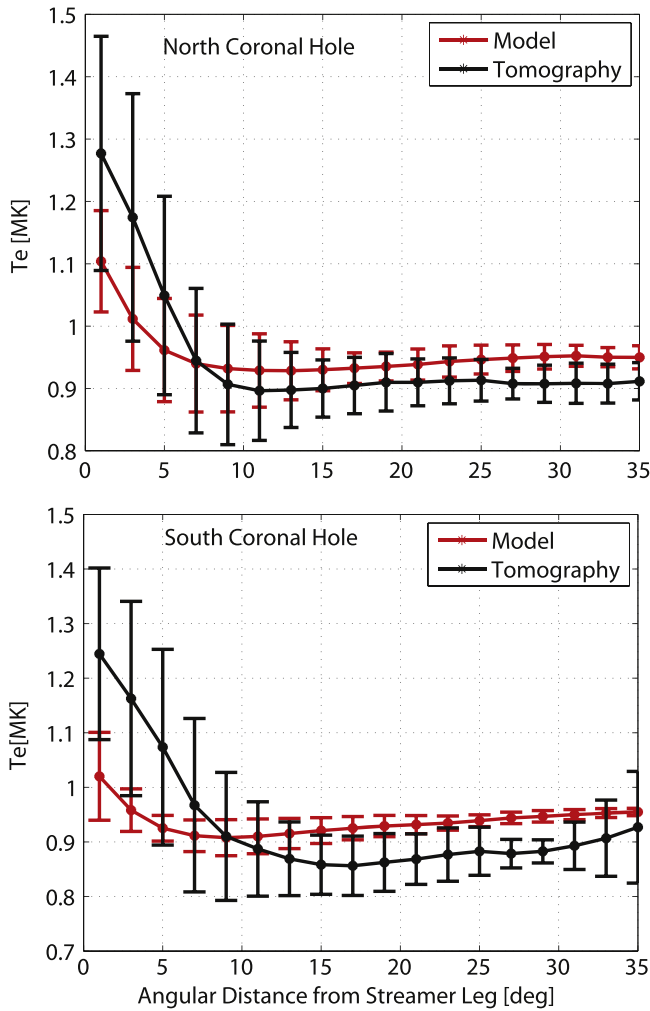
Figure 15. Electron temperature vs. angular distance in the north (top) and south (bottom) coronal holes for CR2063, extracted from the model and tomography density maps at $r = 1.075\,R_{\odot}$. Angular distance is measured from the streamer leg ($0°$) toward the pole ($30°$). The temperature is averaged over all longitudes. The black and red curves show data extracted from tomography and the model, respectively. Error bars show the standard deviation from the averaged values taken from all longitudes.

latitude. The authors did observe an increase in pB at lower latitudes, but this increase was associated with contamination from high-latitude streamer structures that are out of the plane of the sky. This uncertainty in determinations of density from LOS images can be removed to some extent by the DEMT reconstruction used here.

In a DEMT analysis of the latitudinal dependence of the electron density during solar minimum, Vásquez et al. (2010) found it to increase from the CH boundary toward the poles (see their Figure 6). In the present tomographic reconstruction we applied a blind deconvolution of the point-spread function of the EUVI images, using the algorithm developed by Frazin et al. (2012). The results shown in Figures 25 and 26 therein strongly suggest that density variation inside the open field region found by Vásquez et al. (2010) was due to scattered light contamination. The use of the Frazin et al. (2012) algorithm in the present tomographic reconstruction effectively removes this contribution and makes our conclusion that the density varies with latitude more reliable.

We next perform the same statistical analysis for the modeled and reconstructed electron temperature in the polar CHs. The variation of electron temperature as a function of angular distance from the CH edge is shown in Figure 15, for the north (top panel) and south (bottom panel) CHs. The agreement between the model and the reconstructed values is good (as can be clearly seen in the tomographic maps themselves). Both the tomographic reconstruction and the model show that the electron temperature increases toward the edge of the hole. The model underpredicts the temperature in the CHB region, and the agreement improves as we move toward the poles.

In the previous section, we showed that an electron density and temperature enhancement in the CHB region in the lower corona is responsible for the increased charge states in the wind coming from this region. The analysis of the tomographic data confirms that such an enhancement is present on the Sun, and that this behavior is characteristic of the entire CHB region at all longitudes. It also shows that even though the model underpredicts the absolute values in the CHB, it does correctly predict the variation with latitude of these quantities inside the CHB region.

8.4.2. Theoretical Considerations

The formation of enhanced electron density and temperature in the CHB region should be studied rigorously in order to obtain a consistent theoretical picture. This should involve more sophisticated simulations and observations than we used in this work. We here only offer possible conceptual explanations that should be further verified. The simplest explanation is related to the expansion of flux tubes. Those rooted in the CHB region will in general have a larger expansion factor compared to those rooted in the center of the CH. This can lead to two processes that can enhance the electron density. First, the larger expansion will lead to a slower wind coming from the CHB (as can be seen in the bottom panel of Figure 13), which will in turn lead to higher densities. It is not clear, however, by how much it will affect the density at the very low height where the tomography maps were extracted ($r = 1.075\,R_{\odot}$), as the wind speeds at these heights are very low. Second, flux tubes with larger expansion are magnetically connected to a larger volume of the hot corona. This may enable field-aligned electron heat conduction to transport larger amounts of thermal energy back to the chromospheric footpoint. As a result, the energy per unit area reaching the chromosphere in the CHB region will be higher compared to deeper inside the CH. The effects of increased downward heat flux on the density can be viewed in several ways.

In the theoretical work by Hammer (1982a, 1982b), it was shown that an increased downward heat flux from the corona effectively increases the base pressure. This would increase the mass flux into the corona, giving rise to higher densities at larger heights. Increased heat flux may also result in higher rates of chromospheric evaporation (see Klimchuk 2006), whereby heated chromospheric plasma advects upward, supplying the coronal portion of the flux tube with denser material. In both pictures, the increased mass flux can be sustained in steady state due to radiative cooling, which increases with electron density. Thus, radiative cooling works to balance the incoming energy from heat conduction. In steady

state, this will result in a nonuniform transition region, one that reaches different heights for different flux tubes.

A variable transition region height can also occur due to variations in the Alfvén wave Poynting flux, as demonstrated in Suzuki et al. (2013). These authors showed that changing the Poynting flux will result in different fall-off of density with distance. This mechanism is again balanced by radiative cooling. Finally, we note that all the effects above may contribute to the observed enhancement, and a more explicit study should be made to determine their relative contributions.

In the AWSoM model the density at the inner boundary is fixed, and thus it cannot respond to the heat conducted from the corona or to excessive wave heating. In order to determine how the model equations respond to these, a full time-dependent simulation with dynamic boundary condition is required. However, the inclusion of electron heat conduction and radiative cooling allows the present model to mimic the phenomena described above. In a steady state, the heating rate, which is the sum of the local wave heating rate and the heat transport from the corona, is balanced by the radiative cooling rate. As the latter is proportional to the square of the electron density, the steady-state solution will adjust the radial profiles of the electron density accordingly.

9. CONCLUSIONS

The work presented here has combined, for the first time, results from a global 3D model of the solar atmosphere with a heavy ion evolution model, in order to simulate the large-scale latitudinal structure of charge states in the corona and solar wind. Charge states have long been a key observational constraint for theories aiming to explain the processes responsible for the formation and acceleration of the fast and slow solar wind. Any such theory should also explain the observed variations in elemental abundances between the fast and slow solar wind, namely, the appearance of the FIP bias in the slow wind abundances. The AWSoM-MIC simulation presented here cannot address the FIP bias, as the AWSoM model does not describe the separate evolution of the different species and does not incorporate any fractionation mechanism. In addition, the steady-state simulation presented here cannot capture the observed variability in the slow wind properties. However, although this work cannot solve all the open questions regarding the origin of the slow wind, understanding the large-scale structure of charge states in the fast and slow solar wind provides an important piece of the puzzle. The capability to predict charge states from a global model using a realistic magnetic configuration is a major step forward in developing tools to test our understanding of solar wind formation and acceleration, and to ultimately predict space weather.

The main result of this work is that we were able to produce higher levels of the frozen-in charge state ratios O^{7+}/O^{6+} and C^{6+}/C^{5+} in the slow wind compared to those in the fast wind without invoking release of material from the closed field region. We have shown that open flux tubes carrying higher charge state ratios are characterized by lower wind speeds and larger electron densities in the lower corona, where the electron temperature reaches its maximum. These field lines are rooted in a pseudo-streamer, a low-latitude CH, and the boundary region between CHs and the streamer belt. The latter class of field lines are mapped to latitudes between ± 40 in the heliosphere. This means that the boundary region in the model has a higher density compared to deeper inside the CH. The electron density and temperature enhancement was shown to be a global feature of

CHs in the CR under question, both in the global model results and in a tomographic reconstruction of the lower corona.

The theoretical picture presented here of a steady slow wind coming from CHBs does not contradict dynamic release models. Rather, they can be unified. The CHB lines in our steady-state simulation already carry charge state ratios that are consistent with the average level observed in the non-steady slow wind; however, the charge state ratio in the slow wind fluctuates rapidly and can reach values that were not captured by the simulation. Thus, these larger charge state ratios can be due to reconnection of CHB lines with closed field lines at the edges of the streamer belt (a scenario similar to the S-web model presented in Antiochos et al. 2011, 2012). A possible prediction from the work presented here is that the CHB is the source region of a slow, steady, and highly ionized slow wind, but one that exhibits elemental abundances similar to those of CH and the fast wind, that is, without an FIP bias. In an accompanying paper (Stakhiv et al. 2015), this hypothesis was explored observationally by analyzing large amounts of in situ data. Stakhiv et al. (2015) have shown that there is indeed a subset of solar wind flows with high charge states but no FIP bias.

The charge state distributions for Fe, Si, and S below the freeze-in height were used to calculate synthetic emission that was compared to EIS observations in the lower corona, up to 1.115 $R_\odot$ above the limb of a polar CH. Comparing the results for 10 spectral lines suggests that the overall plasma ionization at this height range is too low; emission from low charge state ions was overpredicted, while emission from higher charge states of the same ion was underpredicted. This suggests that the AWSoM wind profiles, and most probably the wind speed below the freeze-in height, need to be improved in order to reach a better agreement. The electron density is also underpredicted in CHs, and this also could cause the wind's ionization state to be lower relative to equilibrium.

We have explored the possible role that supra-thermal electrons can play in charge state evolution. Such an electron population has been hypothesized to be present in the corona, but no direct observational evidence of their existence has been found. We have shown that supra-thermal electrons at ∼3MK making up 2% of the entire electron population can greatly improve the agreement between the predicted and observed charge state levels in the solar wind, consistent with previous work (Ko et al. 1997; Esser & Edgar 2000; Cranmer 2014).

The addition of supra-thermal electrons also improved the agreement between the observed and synthetic fluxes of all 10 emission lines considered here. Thus, we have found a possible observable signature of the presence of supra-thermal electrons in remote spectral observations. This serves as a proof of concept for constraining our estimates of the energy and population size of supra-thermal electrons. Future work should include a parametric study, guided by observations at both ends of the wind trajectory, in order to pin down their properties.

The AWSoM/MIC predictions can be improved by using a more sophisticated description of the solar atmosphere. For example, the wind speed below the freeze-in height can be improved by including a physics-based description of wave reflections (van der Holst et al. 2014). In addition, the effect of differential speeds of the heavy ions can be included by extending the two-temperature MHD description to a multi-fluid MHD description.

REFERENCES

Abbo, L., Antonucci, E., Mikić, Z., et al. 2010, AdSpR, 46, 1400
Alazraki, G., & Couturier, P. 1971, A&A, 13, 380
Antiochos, S. K., DeVore, C. R., Karpen, J. T., & Mikić, Z. 2007, ApJ, 671, 936
Antiochos, S. K., Linker, J. A., Lionello, R., et al. 2012, SSRv, 172, 169
Antiochos, S. K., Mikić, Z., Titov, V. S., Lionello, R., & Linker, J. A. 2011, ApJ, 731, 112
Antonucci, E., Abbo, L., & Telloni, D. 2012, SSRv, 172, 5
Asplund, M., Grevesse, N., Sauval, A. J., & Scott, P. 2009, ARA&A, 47, 481
Bame, S. J., Asbridge, J. R., Feldman, W. C., & Gosling, J. T. 1977, JGR, 82, 1487
Banerjee, D., Gupta, G. R., & Teriaca, L. 2011, SSRv, 158, 267
Belcher, J. W. 1971, ApJ, 168, 509
Bürgi, A., & Geiss, J. 1986, SoPh, 103, 347
Caffau, E., Ludwig, H. G., Steffen, M., Freytag, B., & Bonifacio, P. 2011, SoPh, 268, 255
Cohen, O., Sokolov, I. V., Roussev, I. I., et al. 2007, ApJL, 654, L163
Cranmer, S. R. 2009, LRSP, 6, 1
Cranmer, S. R. 2014, ApJL, 791, L31
Cranmer, S. R., & van Ballegooijen, A. A. 2005, ApJS, 156, 265
Cranmer, S. R., van Ballegooijen, A. A., & Edgar, R. J. 2007, ApJS, 171, 520
Chandran, B. D. G., & Hollweg, J. V. 2009, ApJ, 707, 1659
Culhane, J. L., Harra, L. K., James, A. M., et al. 2007, SoPh, 243, 19
de Pontieu, B., McIntosh, S. W., Carlsson, M., et al. 2007, Sci, 318, 1574
Dere, K. P. 2007, A&A, 466, 771
Dere, K. P., Landi, E., Mason, H. E., Monsignori Fossi, B. C., & Young, P. R. 1997, A&AS, 125, 149
Dere, K. P., Landi, E., Young, P. R., et al. 2009, A&A, 498, 915
Dzifčáková, E. 2006, SoPh, 234, 243
Evans, R. M., Opher, M., Oran, R., et al. 2012, ApJ, 756, 155
Esser, R., & Edgar, R. J. 2000, ApJ, 532, 71
Esser, R., & Edgar, R. J. 2001, ApJ, 563, 1055
Esser, R., Edgar, R. J., & Brickhouse, N. S. 1998, ApJ, 498, 448
Feldman, U., & Laming, J. M. 2000, PhyS, 61, 222
Feldman, U., Landi, E., & Doschek, G. A. 2007, ApJ, 660, 1674
Feldman, U., Mandelbaum, P., Seely, J. F., Doschek, G. A., & Gursky, H. 1992, ApJS, 81, 387
Feldman, U., & Widing, K. G. 2003, SSRv, 107, 665
Ferraro, C. A., & Plumpton, C. 1958, ApJ, 127, 459
Fisk, L. A. 2003, JGRA, 108, 1157
Fisk, L. A., Schwadron, N. A., & Zurbuchen, T. H. 1998, SSRv, 86, 51
Fisk, L. A., & Zhao, L. 2009, in IAU Symp. 275, Universal Heliophysical Processes, ed. N. Gopalswamy & D. F. Webb (Cambridge: Cambridge Univ. Press), 109
Frazin, R. A., Kamalabadi, F., & Weber, M. A. 2005, ApJ, 628, 1070
Frazin, R. A., Vásquez, A. M., & Kamalabadi, F. 2009, ApJ, 701, 547
Freeland, S. L., & Handy, B. N. 1998, SoPh, 182, 497
Geiss, J., Gloeckler, G., & von Steiger, R. 1995, SSRv, 72, 49
Gloeckler, G., Geiss, J., Balsiger, H., et al. 1992, A&AS, 92, 267
Gloeckler, G., Zurbuchen, T. H., & Geiss, J. 2003, JGRA, 108, 1158
Gosling, J. T. 1997, in AIP Conf Ser. 385, Robotic Exploration Close to the Sun: Scientific Basis, ed. S. R. Habbal (Melville, NY: AIP), 17
Gruesbeck, J. R., Lepri, S. T., Zurbuchen, T. H., & Antiochos, S. K. 2011, ApJ, 730, 103
Guhathakurta, M., & Holzer, T. E. 1994, ApJ, 426, 782
Hahn, M., Bryans, P., Landi, E., Miralles, M. P., & Savin, D. W. 2010, ApJ, 725, 774

Hahn, M., Landi, E., & Savin, D. W. 2012, ApJ, 753, 36
Hammer, R. 1982a, ApJ, 259, 767
Hammer, R. 1982b, ApJ, 259, 779
Hollweg, J. V. 1986, JGR, 91, 4111
Howard, R. A., Moses, J. D., Vourlidas, A., et al. 2008, SSRv, 136, 67
Hundhausen, A. J., Gilbert, H. E., & Bame, S. J. 1968, JGR, 73, 5485
Jin, M., Manchester, W. B., van der Holst, B., et al. 2012, ApJ, 745, 6
Jin, M., Manchester, W. B., van der Holst, B., et al. 2013, ApJ, 773, 50
Klimchuk, J. A. 2006, SoPh, 234, 41
Ko, Y.-K., Fisk, L. A., Geiss, J., Gloeckler, G., & Guhathakurta, M. 1997, SoPh, 171, 345
Ko, Y.-K., Geiss, J., & Gloeckler, G. 1998, JGR, 103, 14539
Kohl, J. L., Noci, G., Cranmer, S. R., & Raymond, J. C. 2006, A&ARv, 13, 31
Kovalenko, V. A. 1981, SoPh, 73, 383
Laming, J. M. 2004, ApJ, 614, 1063
Laming, J. M. 2009, ApJ, 695, 954
Laming, J. M. 2012, ApJ, 744, 115
Laming, J. M., & Lepri, S. T. 2007, ApJ, 660, 1642
Landi, E. 2007, ApJ, 663, 1363
Landi, E., Gruesbeck, J. R., Lepri, S. T., & Zurbuchen, T. H. 2012a, ApJ, 750, 159
Landi, E., Gruesbeck, J. R., Lepri, S. T., Zurbuchen, T. H., & Fisk, L. A. 2012b, ApJ, 761, 48
Landi, E., Oran, R., Lepri, S. T., et al. 2014, ApJ, 790, 111
Landi, E., Young, P. R., Dere, K. P., del Zanna, G., & Mason, H. E. 2013, ApJ, 763, 86
Lepri, S. T., & Zurbuchen, T. H. 2004, JGRA, 109, A01112
Lepri, S. T., Zurbuchen, T. H., Fisk, L. A., et al. 2001, JGR, 106, 29, 231
Lionello, R., Velli, M., Downs, C., et al. 2014a, ApJ, 784, 120
Lionello, R., Velli, M., Downs, C., Linker, J. A., & Mikić, Z. 2014b, ApJ, 796, 111
Matthaeus, W. H., Zank, G. P., Oughton, S., Mullan, D. J., & Dmitruk, P. 1999, ApJ, 523, 93
McComas, D. J., Barraclough, B. L., Funsten, H. O., et al. 2000, JGR, 105, 10419
McComas, D. J., Elliott, H. A., Schwadron, N. A., et al. 2003, GeoRL, 30, 1517
McIntosh, S. W., de Pontieu, B., Carlsson, M., et al. 2011, Natur, 475, 477
Oran, R., Landi, E., van der Holst, B., Sokolov, I. V., & Gombosi, T. I. 2014, arXiv:1401.0565
Oran, R., van der Holst, B., Landi, E., et al. 2013, ApJ, 778, 176
Roussev, I. I., Gombosi, T. I., Sokolov, I. V., et al. 2003, ApJL, 595, L57
Scherrer, P. H., Bogart, R. S., Bush, R. I., et al. 1995, SoPh, 162, 129
Schwenn, R., & Marsch, E. 1990, PCS, 20, 1
Shearer, P., Frazin, R. A., Hero, A. O., III, & Gilbert, A. C. 2012, ApJL, 749, L8
Sokolov, I. V., van der Holst, B., Oran, R., et al. 2013, ApJ, 764, 23
Stakhiv, M., Landi, E., Lepri, S. T., Oran, R., & Zurbuchen, T. H. 2015, ApJ, 801, 100
Suess, S. T. 1979, SSRv, 23, 159
Suess, S. T., Ko, Y.-K., von Steiger, R., & Moore, R. L. 2009, JGRA, 114, A04103
Suzuki, T. K. 2006, ApJL, 640, L75
Suzuki, T. K., Imada, S., Kataoka, R., et al. 2013, PASJ, 65, 98
Usmanov, A. V., & Goldstein, M. L. 2003, JGR, 108, 1354
Usmanov, A. V., Goldstein, M. L., Besser, B. P., & Fritzer, J. M. 2000, JGR, 105, 675
Usmanov, A. V., Goldstein, M. L., & Matthaeus, W. H. 2012, in AIP Conf. Proc. 1436, Physics of the Heliosphere, ed. J. Heerikhuisen, G. Li, N. Pogorelov, & G. Zank (Melville, NY: AIP), 344
van Ballegooijen, A. A., Asgari-Targhi, M., Cranmer, S. R., & DeLuca, E. E. 2011, ApJ, 736, 3
van der Holst, B., Manchester, W. B., IV, Frazin, R. A., et al. 2010, ApJ, 725, 1373
van der Holst, B., Sokolov, I. V., Meng, X., et al. 2014, ApJ, 782, 81
Vásquez, A. M., Frazin, R. A., & Manchester, W. B., IV 2010, ApJ, 715, 1352
von Steiger, R., Schwadron, N. A., Fisk, L. A., et al. 2000, JGR, 105, 217
von Steiger, R., Schweingruber, R. F. W., Geiss, J., & Gloeckler, G. 1995, AdSpR, 15, 3
von Steiger, R., Zurbuchen, T. H., Geiss, J., et al. 2001, SSRv, 97, 123
Wang, Y.-M., & Sheeley, N. R. 1990, ApJ, 355, 726
Wang, Y.-M., Sheeley, N. R., Socker, D. G., Howard, R. A., & Rich, N. B. 2000, JGR, 105, 133
Warren, H. P., Ugarte-Urra, I., & Landi, E. 2014, ApJS, 213, 11
Withbroe, G. L. 1988, ApJ, 325, 442

Zhao, L., Landi, E., Zurbuchen, T. H., Fisk, L. A., & Lepri, S. T. 2014, ApJ, 793, 44

Zhao, L., Zurbuchen, T. H., & Fisk, L. A. 2009, GeoRL, 36, L14104

Zurbuchen, T. H. 2001, in IAU Symp. 203, Recent Insights into the Physics of the Sun and Heliosphere: Highlights from *SOHO* and Other Space Missions, ed. P. Brekke, B. Fleck, & J. B. Gurman (San Francisco, CA: ASP), 585

Zurbuchen, T. H. 2007, ARA&A, 45, 297

Zurbuchen, T. H., Fisk, L. A., Gloeckler, G., & von Steiger, R. 2002, GeoRL, 29, 1352

Zurbuchen, T. H., Hefti, S., Fisk, L. A., Gloeckler, G., & von Steiger, R. 1999, SSRv, 87, 353

Zurbuchen, T. H., & von Steiger, R. 2006, in ESA Special Publication 617, *SOHO*-17. 10 Years of *SOHO* and Beyond ed. H. Lacoste & L. Ouwehand, CD-ROM, id.7.1